Design Modification in Single-Tooth Winding Double-Stator Switched Reluctance Motor for Torque Ripple Mitigation

**TRIPURARI DAS GUPTA[1,2], KALPANA CHAUDHARY[1], (Senior Member, IEEE),
RAJVIKRAM MADURAI ELAVARASAN [3], R. K. SAKET [1], (Senior Member, IEEE),
IRFAN KHAN [3], (Senior Member, IEEE), AND
EKLAS HOSSAIN [4], (Senior Member, IEEE)**

[1]Department of Electrical Engineering, India Institute of Technology (BHU) Varanasi 221005, India
[2]Department of Electrical and Electronics Engineering, Nalanda College of Engineering, Nalanda 803108, India
[3]Clean and Resilient Energy Systems (CARES) Laboratory, Texas A&M University, Galveston, TX 77553, USA
[4]Department of Electrical Engineering and Renewable Energy, Oregon Renewable Energy Center (OREC), Oregon Institute of Technology, Klamath Falls, OR 97601, USA

Corresponding authors: Rajvikram Madurai Elavarasan (rajvikram787@gmail.com) and R. K. Saket (rksaket.eee@iitbhu.ac.in)

ABSTRACT Double-stator switched reluctance motors (DSSRMs) with single-tooth winding topology possesses high torque density when compared to conventional switched reluctance motors (SRMs). However, their inherent high torque ripple is still an issue for industrial applications. In SRMs, the torque shared by the outgoing phase reduces significantly in the commutation region. However, at the same time, the incoming phase does not achieve sufficient torque generation. This results in a high torque ripple in this region. In this paper, several design procedures are discussed to improve the performance of the radial flux DSSRM with single-tooth winding topology. Firstly, the pole arc equations of stator pole and rotor segments for the higher difference between aligned and unaligned inductance are derived for high output torque and based on this, the selection of the number of stator slots/rotor segments is discussed. Furthermore, the influence of winding polarities on the core loss and output torque of DSSRM is discussed. Finally, the design modification in rotor structure is proposed with an angular shift in the alternate rotor segments in the direction of rotation to mitigate the torque ripple. To investigate the effectiveness of the proposed design modification, a finite-element model of a 3-phase 12/10/12 pole radial flux DSSRM is developed in ANSYS/MAXWELL software, and simulation results are presented. It is observed that a 40% reduction in the torque ripple is achieved in the case of the proposed motor. The proposed design modification improves the torque generating capability of the incoming phase in the commutation region, which reduces the torque dip in this region and subsequently reduces the torque ripple.

INDEX TERMS Electrical machine, finite-element analysis, switched reluctance motor, torque ripple.

I. INTRODUCTION

In the growing demand of high-performance electrical machines (EMs), permanent magnet (PM) machines currently prevail as a primary choice because of their high torque/power density and high efficiency [1]–[3]. However, because of their limited resources, unstable cost and fault-tolerant issues, the researchers are interested in an attractive alternative to PM based motors. Switched reluctance motors (SRMs) are gaining much attention in

The associate editor coordinating the review of this manuscript and approving it for publication was Xiaodong Liang [ID].

several applications because of their simple construction, fault-tolerant capability, ability to work in harsh environments, absence of PM and wide speed range [4]–[8]. The advances in power electronics circuits further increase their suitability for a wide variety of applications such as agricultural applications [9], aircraft applications [10] and household appliances [11], [12]. However, the issues of lower efficiency, lower torque/power density and high torque ripple demand further improvements for their adoption in industrial applications. To improve these performance parameters, several research articles have been reported in the earlier literature works [13]–[15]. The use of high-quality iron steel

and a high slot fill factor improves efficiency by 6% [13]. P. Desai *et al.* [14] reported that in toothed SRM (TSRM) higher torque is generated with a higher number of rotor poles than stator poles. B. C. Mecrow *et al.* [15] have evaluated the performance of segmented rotor SRM (SSRM) with single-tooth winding topology and reported that this machine has a compact size, lower copper volume, increased flux linking per turn; and subsequently improves the torque output as compared to full-pitch winding SRMs. There have been several patents filed which highlight the continuous improvements and potentiality of SRMs technology [16]–[18]. In patent [16], a segmented external rotor SRM has been claimed with the objectives of a hub motor for an electric vehicle having advantages of high torque, high efficiency, compact size and a suitable substitute for brushless DC motor. In patent [17], a simple and improved SRM drive with 2-phase 30/45 poles low flux path pattern has been claimed for the application of hybrid electric vehicles. In patent [18], an SRM with permanent magnets mounted between the adjacent stator poles has been claimed with improved efficiency with lower back EMF. Double-stator SRMs (DSSRMs) emerges as a new SRM topology with two stators which exhibits further improvement in torque to active weight ratio, lower vibration and lower acoustic noise. Some recent research works provide further performance improvements and comparisons in DSSRM. The winding topology suggested in [15] is further extended to DSSRM in [19], which improves the efficiency and lowers the heat losses because of which high efficiency in the wider speed region is plausible. E. Bostanci *et al.* [20] analysed the performance of DSSRM having single-tooth winding and found it competitive with the interior PM (IPM) motors for electric vehicles application. To extend the wide speed operation with less frictional loss, bearingless SRM is suggested in [21]. To solve the coupling problem of DSSRMs, a new double-stator bearingless SRM is proposed in [22] which has the self-decoupling property between torque and suspension system that ultimately improved the torque/suspension output.

Due to the doubly salient structure and discrete excitation of phases, SRMs generally have high torque ripple. To reduce the vibration, acoustic noise and torque ripple, skewing of stator and rotor surface by an angle of 22.5° for a 12/8 pole TSRM have been reported [23]. It has been reported in research that increasing the phase number reduces the torque ripple [24], [25]. In [24], for low torque ripple, a 6-phase SSRM is considered with standard VSI for its drive circuit. However, this system requires 6 extra diodes connected with its phase windings. A new drives system has been proposed in [25] to reduce the torque ripple in a 6-phase SRM, which does not require any additional component as compared to the conventional half-bridge converter. In [26], various shifting techniques of adjacent PMs are investigated to reduce the torque ripple due to cogging in an axial flux PM (AFPM) motor. In an axial flux dual-rotor, single-stator SRM [27] and an axial flux double-sided SRM [28], the adjacent rotor segments/poles are shifted in the opposite direction to reduce

the torque ripple. However, the axial flux machines have higher manufacturing complexity and cost as compared to the radial flux machines. In [29], the arc angles of stator and rotor poles of a 12/8/12 pole DSSRM are optimized for 15° rotor position range through static parametric analysis for torque ripple reduction and high torque output. N. Tojima *et al.* filed a patent [30], with a DSSRM with salient poles on inner and outer stators and both sides of the rotor surfaces. It has been claimed that if the phase shift is given with half of the stroke angle either between inner and outer stator poles or the poles of inner and outer rotor surfaces, torque ripple is reduced.

As compared to the previously reported works in [31] and [32], several design techniques have been suggested and investigated in this study to further improve the performance of DSSRM. In this study, an analytical design procedure for single-tooth winding DSSRMs has been presented whose characteristics include higher fault-tolerant capability and compact structure in relative to full pitch windings motors. Moreover, the stator and rotor pole arc angles are derived for obtaining the higher difference between aligned and unaligned inductance to increase the output torque. Based on these criteria, the selection of the number of stator pole/rotor segments is discussed. The influence of winding polarities on the flux density of different motor parts is presented and its effects on core loss and output torque of the motor are investigated. Finally, the methodology to reduce torque ripple through the shift of alternate rotor segments is suggested and investigated. The effect of segment shift on flux distributions and its influences on motor performance as well as a radial force have also been examined. A detailed analysis of this technique is carried out for a 3-phase 12/10/12 pole radial flux DSSRM. In order to investigate the effectiveness of the proposed design modification, a finite-element method (FEM) based model is developed in ANSYS/MAXWELL software and simulation results are presented.

The paper is organized as follows: constructional details of DSSRM with single-tooth winding are discussed in Section II. Section III deals with the analytical design procedure of DSSRM. The selection of the number of stator poles/rotor segments combination is presented in Section IV. The influence of winding polarities on core loss and output torque are detailed in Section V. The schematic of torque ripple reduction through rotor segments shift in the proposed motor is elaborated in Section VI. FEM modeling and simulation results are presented in Section VII. Subsequently, the conclusions are provided in Section VIII.

II. SRM TOPOLOGY
A. CONVENTIONAL SRM TOPOLOGY
The construction of conventional SRMs is one of the simplest configurations among all the electrical machines (EMs). Fig. 1 shows a 3-phase 12/8 pole SRM with only phase A windings shown. Phase B and phase C windings will be 30° and 60° mechanically apart from phase A, respectively. The windings are present on each stator pole viz. P_{A1}, P_{B1},
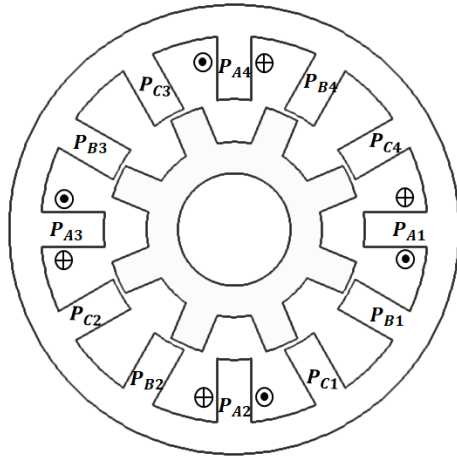
FIGURE 1. Conventional 12/8 pole SRM with phase A winding.

P_{C1}, ... P_{A4}, P_{B4}, P_{C4} respectively. Therefore, each stator slot places the conductors of two adjacent phases. The position of the rotor, as in Fig. 1, is in a completely unaligned condition with that of phase A. If phase A is energized, the rotor will try to align with the magnetic field with this phase. If the phases are energized in the sequence of ABC, the rotor will start rotating in the counter-clockwise direction.

B. SINGLE-TOOTH WINDING DSSRM TOPOLOGY

DSSRMs have higher torque/power density as compared to conventional SRMs because of better utilization of machine volume with the insertion of the segmented rotor and secondary stator. In a radial flux DSSRM, a segmented rotor is placed between two stators; inner and outer, and shares the magnetic fluxes of both. Fig. 2 shows the structure of a 3-phase 12/10/12 pole DSSRM with single-tooth winding topology. Fig. 2 (a) shows the its cross-sectional view with only phase A windings shown. Fig. 2 (b) shows its exploded view. As the name suggests, each stator has 12 stator poles and the rotor has 10 segments. The stator poles are categorized into two types which are exciting poles (viz. P_{A1}, P_{B1}, P_{C1}, ...P_{A4}, P_{B4}, P_{C4}) and auxiliary poles. The phase windings are only wound on the exciting poles whereas no windings are present on the auxiliary poles. The auxiliary poles only provide the return paths for the flux generated by the exciting poles. The poles of inner and outer stators are in face alignment. The rotor is made of discrete segments that are magnetically isolated from each other and embedded into a nonmagnetic isolator. In Fig. 2, it can be seen that in single-tooth winding topology each stator slot contains the conductors of only one phase, subsequently, this winding topology has a compact structure and thus, expresses more fault-tolerant capability. The polarity of the inner stator and outer stator coils of a phase is selected in such a way that they create flux cancellation characteristics near the unaligned rotor position. This characteristics of the machine decreases the unaligned inductance and increases the output torque.
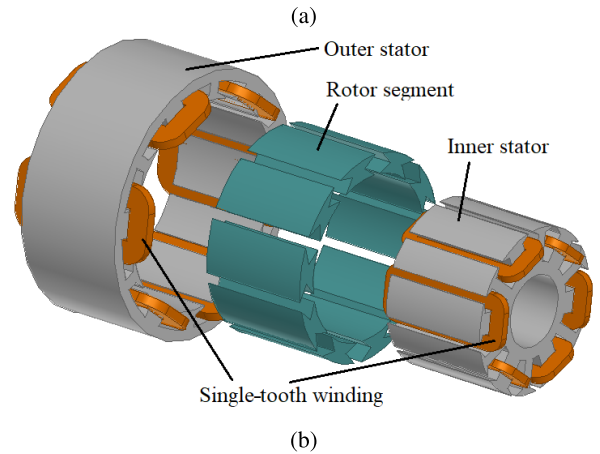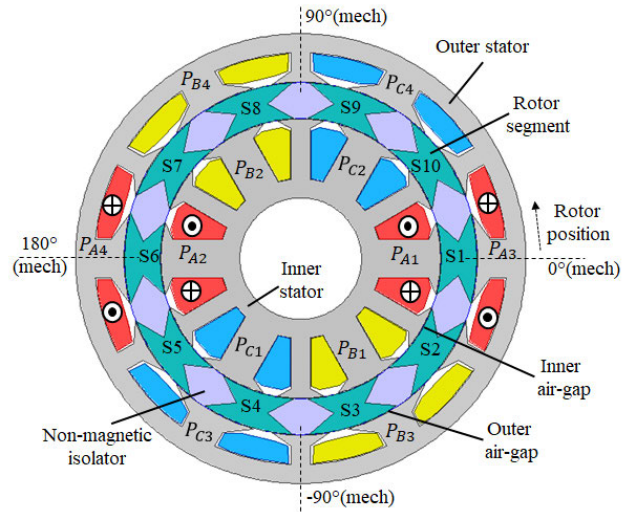

(a)

(b)

FIGURE 2. Structure of 3-phase 12/10/12 pole DSSRM with single-tooth winding. (a) Cross-sectional view with only phase A windings. (b) Exploded view.

In Fig 2 (a), the rotor is shown in an unaligned position with phase A and also defined as 0° mechanical position. For each phase excitation, 4 different rotor segments come into the magnetic influence of it (viz. S1, S2, S6 and S7 for phase A), and rotor will try to magnetically align with the excited phase. Hence, the rotor can start rotating in the counter-clockwise direction if the phases are energized in the sequence of ABC.

Fig. 3 shows the magnetic flux distributions of the DSSRM for unaligned and aligned rotor position, respectively, for an excited phase. The magnetic flux flows from the exciting stator poles and returns through the adjacent auxiliary poles passing via rotor segments. The flux paths are shorter in this structure, therefore increases the electrical utilization of the machine. Furthermore, the figure also represents the flux cancellation characteristics near the unaligned rotor position, which reduces the unaligned inductance.

III. DESIGN PROCEDURE OF DSSRM

In this section, the design methodology of the single-tooth winding DSSRM has been presented. The SRMs show a
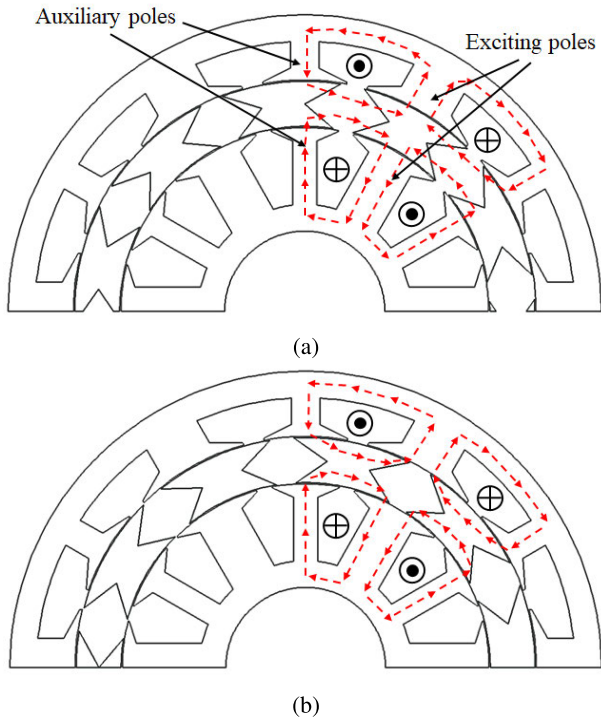
(a)

(b)

FIGURE 3. Magnetic flux distributions of DSSRM. (a) Unaligned position. (b) Aligned position.

non-linear variation in its performance with respect to the variation in its design parameters. Therefore, FEM based simulation study is utilized to yield an accurate design procedure.

A. TORQUE EQUATION

The instantaneous torque developed in an SRM as given by [33]

$$t = \frac{1}{2} i^2 \frac{dl}{d\theta} \tag{1}$$

The average torque developed in the motor is as given below

$$T_{avg} = \frac{1}{2} I_p^2 \frac{(L_a - L_u)}{\frac{2\pi}{(N_r \, q)}} \tag{2}$$

or

$$T_{avg} = \frac{1}{4\pi} I_p^2 L_a \left(1 - \frac{L_u}{L_a}\right) N_r \, q \tag{3}$$

where I_p is the peak value of phase current, L_u and L_a are the unaligned and aligned phase inductances respectively, N_r is the number of rotor segments and q is the total number of phases. The per-phase inductance at the aligned position is given as

$$L_a = \frac{N_{ph} \, B_g \, A_{ol}}{I_p} \tag{4}$$

The air-gap flux density B_g at the aligned rotor position is

$$B_g = \frac{N_{ph} \, I_p \, \mu_0}{8 \times m \times l_g} \tag{5}$$

where N_{ph} is the number of turns per phase, l_g is the length of inner and outer air-gaps and m is the multiplicity of the motor.

Substituting Eq. (4) in Eq. (3); the average torque of the DSSRM is expressed as

$$T_{avg} = \frac{1}{4\pi} N_{ph} \, I_p \, B_g \, A_{ol} \left(1 - \frac{L_u}{L_a}\right) N_r \, q \tag{6}$$

The overlap area A_{ol} between the stator poles and rotor segments surfaces in aligned position is

$$A_{ol} = (A_{ol \, inner} + A_{ol \, outer})$$
$$A_{ol} = \frac{\pi (D_{ri} + D_{ro}) \times l}{N_r \, q}$$
$$A_{ol} = \frac{2\pi \times D_r \times l}{N_r \, q} \tag{7}$$

Substituting Eq. (7) in Eq. (6) we obtain

$$T_{avg} = \frac{1}{2} N_{ph} \, I_p \, B_g \left(1 - \frac{L_u}{L_a}\right) D_r \, l \tag{8}$$

$$T_{avg} = \frac{1}{2} N_{ph} \, I_p \, B_g \, k \, D_r \, l \tag{9}$$

where $D_r = (D_{ri} + D_{ro})/2$ is the average diameter of the rotor, l is the axial length of the motor and $k = (1 - L_u/L_a)$ which can be calculated by FEM based simulation results.

It is seen in Eq. (8) that for a given MMF and magnetic loading B_g, the average torque depends on the average diameter of rotor (D_r), axial length (l) of motor and the aligned and unaligned inductances of the phase windings. The value of D_r is dependent on the outer diameter of motor and pole heights the stators. It is clear that a higher output torque is obtained for a higher value of aligned inductance and lower value of unaligned inductance. Therefore, during the design procedure, the proper selection of these parameters is essential to obtain the higher output torque.

B. SIZING PROCEDURE

Fig. 4 shows the half cross-sectional view and a cut view of an approximated linear model of a DSSRM showing the different dimensions and parameters of the machine. Fig. 4 (a) shows the outer and inner diameter of the motor (D_o, D_i), the average diameter of rotor (D_r), stator and rotor pole pitch angles (β_{ps}, β_{pr}), stator and rotor slot opening angles (β_{so}, β_{ro}) and arc angles of exciting, auxiliary poles and rotor segments ($\beta_{exc}, \beta_{aux}, \beta_r$). Fig. 4 (b) shows the dimensions of different magnetic parts of stator and rotor. Since the yoke of inner and outer stator bear nearly the same level of magnetic flux density, they have the same width of h_{ys}. As seen in Fig. 3, the flux passing through an exciting pole of a stator is distributed between two adjacent auxiliary poles. Therefore, the width of the exciting poles (w_{exc}) is twice the width of the auxiliary poles (w_{aux}). Moreover, the flux passing through the yoke of a stator subsequently passes through the auxiliary pole and thereafter half of the height of the rotor segment (h_{pr}). The above field distribution reveals the following conclusions:
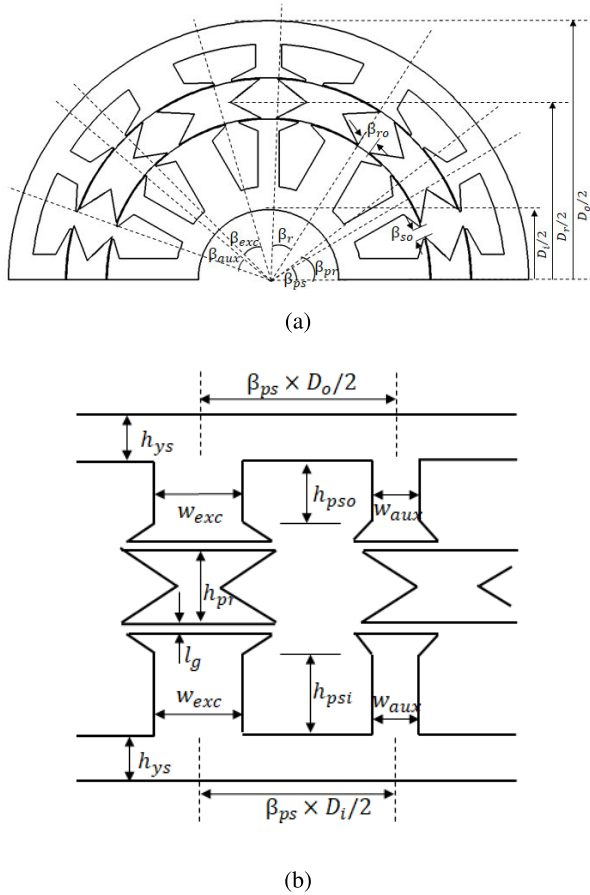
$$w_{exc} = 2 \, h_{ys} \tag{10}$$

(a)

(b)

FIGURE 4. (a) Half section of the 2-D view. (b) Cut view of approximated linear model.

$$w_{aux} = h_{ys} \tag{11}$$

and

$$h_{pr} \simeq 2 \, h_{ys} \tag{12}$$

From the above equations, it is observed that the selection of height of stator yoke (h_{ys}) is very important for the design as other parameters are linearly dependent on it. To increase the output torque of the machine, the MMF/slot should be increased ensuring that the maximum flux density in different parts of the machine is within the maximum permissible limit, B_{max}. This requires to increase the value of h_{ys} with the increase in MMF/slot. To share equal torque and power by inner and outer stators, the MMF/slot for inner and outer stator slots should be same. This will also reduce the radial force on rotor segments because nearly equal and opposite radial force will be exerted on the rotor segments. As the inner stator has an enclosed surrounding, poor heat dissipation condition may prevail which can affect its thermal stability and hence, the power density. Therefore, a better cooling arrangement is required to impart thermal stability. The problem of heat dissipation in inner stator can be reduced by decreasing the current density in its windings. This will

require higher conductor cross-sectional area and higher slot area for inner stator windings for a given MMF. An increase in the slot area will require increase in the pole height of the inner stator (h_{psi}). Increasing the pole height will further lead to an increase in the motor weight which will reduce the torque/power density of the motor. However, this arrangement will reduce the heat dissipation issue and will improve the thermal stability of the machine. In higher outer diameter machines there is more flexibility to increase the height of inner stator poles. Therefore, in such machines, the lower current density in inner stator windings can be adopted to improve its thermal stability.

C. CALCULATION OF STATOR POLE/ROTOR SEGMENT ARC ANGLES

The output torque of an SRM is high for the higher value of the difference between aligned and unaligned inductances. For minimum unaligned inductance, the nonmagnetic separation between two adjacent rotor segments (β_{ro}) should not be lesser than the stator slot opening angle (β_{so}). Moreover, the arc angle of rotor segments (β_r) should not be greater than the arc angle of exciting stator poles (β_{ext}). Therefore, the minimum unaligned inductance can be assured by the following two conditions:

$$\beta_{ro} \geq \beta_{so} \tag{13}$$

and

$$\beta_r = \beta_{exc} \tag{14}$$

The graphical representation for the minimum unaligned inductance condition is given in Fig. 5 (a). The condition of maximum aligned inductance can be achieved when the rotor segments overlap area with the exciting and auxiliary poles are equal in aligned rotor position. The graphical representation for this condition is provided in Fig. 5 (b). In this case, the arc *AB* and arc *PQ* have equal span at the aligned condition. This condition can be assured by the following expression:

$$\beta_{exc} - \beta_{aux} = 2 \times (360°/N_r - \beta_{ps}) \tag{15}$$

Another geometric relationship between the exciting and auxiliary pole arc angles for a given stator slot opening angle of β_{so} is:

$$\beta_{exc} + \beta_{aux} = 2 \times (360°/N_s - \beta_{so}) \tag{16}$$

where β_{exc} and β_{aux} are in degree; N_r and N_s are the number of rotor segments and stator poles respectively. Considering the above constraints the values of β_{exc}, β_{aux} and β_r are as follows:

$$\beta_{exc} = \beta_{pr} - \beta_{so} \tag{17}$$
$$\beta_{aux} = 2\beta_{ps} - \beta_{pr} - \beta_{so} \tag{18}$$

and

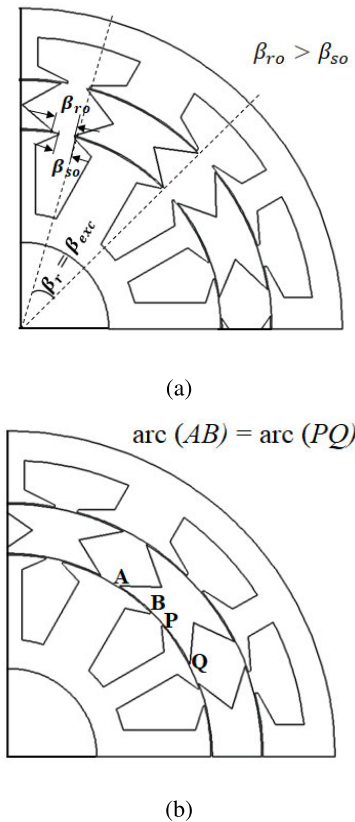$$\beta_r = \beta_{pr} - \beta_{so} \tag{19}$$

(a)

arc (AB) = arc (PQ)

(b)

FIGURE 5. Condition for minimum unaligned and maximum aligned inductances. (a) Minimum unaligned inductance condition. (b) Maximum aligned inductance condition.

FIGURE 6. Flowchart for the design procedure of DSSRM.

TABLE 2. Initial design parameters for rated operation.

Parameter	Value
Number of phases (q)	3
Outer diameter(D_o)	200 mm
Maximum axial length (l_m)	90 mm
Rated power (P_o)	2.5 KW
Rated Speed (N)	600 rpm
Rated torque (T_{avg})	40 N-m

During the design of DSSRM, the height of stator yoke h_{ys} and pole height of inner and outer stator can be calculated by FEM base simulation study in such a way that maximum flux density in different parts of the machine should be within B_{max}. In this paper, B_{max} is considered within 1.8 T and flux density in various magnetic parts of the motor in the aligned position is in the range of 1.7 T. The dimensions of other parts of DSSRM can be calculated using Eq. (10)-(12) and Eq. (17)-(19). The flowchart for the design procedure of DSSRM is shown in Fig. 6.

TABLE 1. Valid slot/segment combinations for 3-phase DSSRM with single-tooth winding.

No. of phases (q)	Multiplicity (m)	Slot/segment combination
3	1	6/4,6/5,6/7 etc.
3	2	12/8,12/10,12/14 etc.

IV. SELECTION OF THE NUMBER OF STATOR SLOTS/ROTOR SEGMENTS

To select the number of stator pole and rotor segments for a 3-phase DSSRM, the valid slot/segment combinations are listed in Table 1. The combinations with unity multiplicity ($m = 1$) are not considered because of unbalanced magnetic
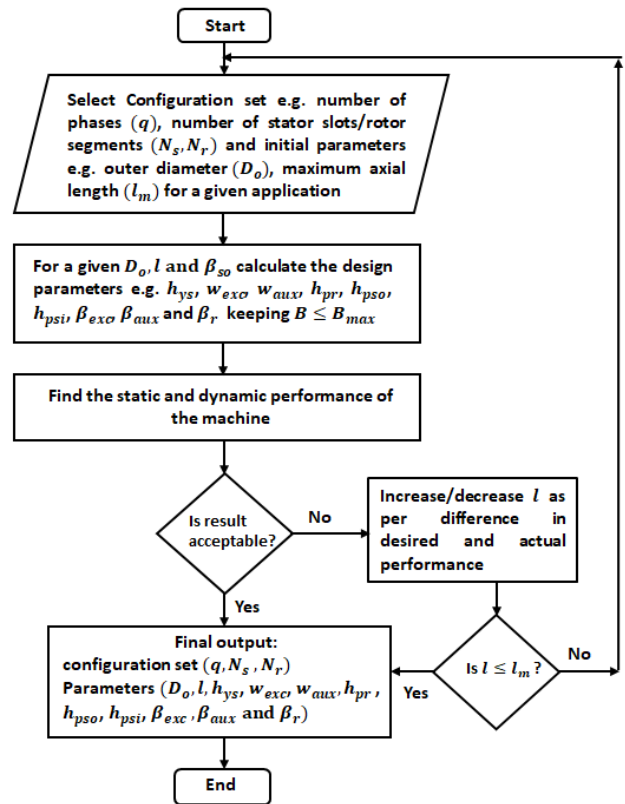
forces on the stator surfaces. The combinations of 12/8, 12/10 and 12/14 poles with twice multiplicity are considered for comparison in the view of axial length requirement, unaligned/aligned inductances and total active weight of the machine. Table 2 lists the rated operating condition for the comparison of considered slot/segments combinations with the constraints as given in Eq. (17)-(19).

The stator slot opening angle β_{so} is considered in the range of 5°- 6°. The value of β_{so} for 12/8 and 12/10 pole combinations is 6°. However, because of the increase in the number of rotor segments in 12/14 pole combination, β_r reduces considerably. This will reduce the overlapping of rotor segments with exciting and auxiliary poles at the aligned condition and reduces the aligned inductance. Therefore, to increase the aligned inductance, the value of β_{so} is reduced to 5° for this combination. The performance comparison of the different combinations has been done for a 5 A/mm2 of average phase

current with slot fill factor (SFF) of 0.43. In the concern of current density, the same average current density has been provided to each motor by providing a trapezoidal current wave of 35° (elec.) rising and falling period and 110° (elec.) period of rated value which is 26 A for each motor. The same MMF/slot and same conductor cross-section are considered for inner and outer stator windings. The frequency of current switching per revolution for 12/8, 12/10, and 12/14 pole motor taken are 24, 30, and 42, respectively; and results are listed in Table 3.

TABLE 3. Comparison between different slot/segment combinations of DSSRM.

Parameter	12/8 pole	12/10 pole	12/14 pole
Torque T_{avg} in N-m	40.7	40.3	40.5
Axial length (l) in mm	106	85	94
Unaligned inductance(L_u) in mH	4.39	3.39	4.85
Aligned inductance (L_a) in mH	25.80	21.10	17.39
Iron weight in kg	14.36	11.61	12.54
Copper weight in kg	3.23	2.76	3.10
Total active weight in kg	17.59	14.37	15.64

It is observed that the axial length required for the rated torque generation in 12/10 pole combination is 85 mm which is nearly 8/10 times of the 12/8 pole combination. This is because of the higher number of strokes per revolution in 12/10 pole combination as compared to 12/8 pole, which increases the torque density in it. This is the same case as in conventional SRM where the output torque increases with the increase in the number of rotor poles. Furthermore, because of the higher axial length, the value of L_u, L_a and total active weight is high in 12/8 pole machine as compared to 12/10 pole combination. With the further increase in the number of rotor segments, in 12/14 pole combination, the condition as given in Eq. (13) is violated, subsequently the assurance of minimum inductance and maximum reluctance at unaligned position diminishes. The value of L_u increases and torque density reduces. Therefore, the benefit of a higher number of strokes per revolution becomes ineffective in this case. The axial length required for rated torque generation increases to 94 mm in this case, subsequently, the total active weight of the machine also increases. Therefore, for the rated operation, 12/10 pole combination has better performance over others and is considered for further analysis in this paper.

V. INFLUENCE OF WINDING POLARITY ON DSSRM PERFORMANCE

In SRMs, two phases are excited at the same time during the commutation period to increase the output torque and to reduce torque ripple. However, the excitation patterns of two consecutive phase windings have different influence on its performance. Fig. 7 shows the possible winding polarities for 12/10 pole DSSRM. Fig. 7 (a) shows the aiding flux winding polarity in which the fluxes of two adjacent phases are in the same direction in the auxiliary pole and it carries the summation of the fluxes. This winding pattern has no flux
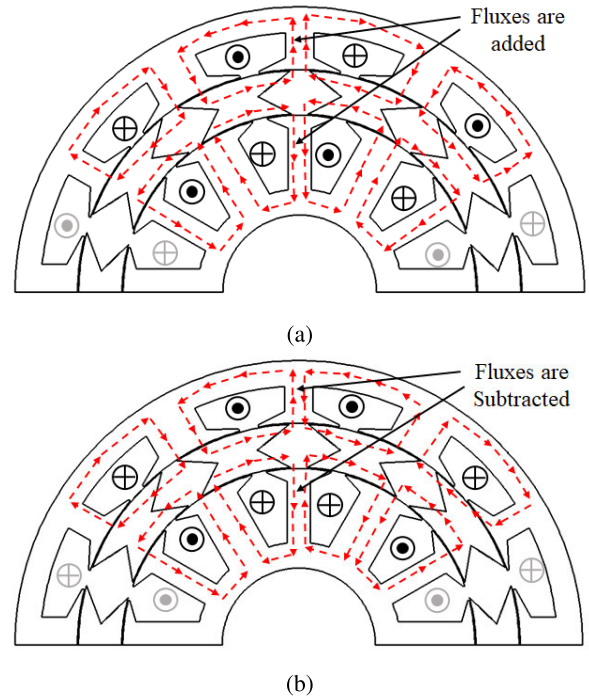

(a)

(b)

FIGURE 7. Simultaneous excitation of two phases. (a) Aiding flux winging polarity. (b) Subtracting flux winding polarity.

reversal in the auxiliary poles, which reduces the core losses. However, there may be saturation in the auxiliary poles which reduces the output torque. Fig. 7 (b) illustrates the subtracting flux winding polarity in which the fluxes of two adjacent phases are in opposite direction in the auxiliary pole and it carries the difference of the fluxes. This winding pattern will reduce the saturation condition in the auxiliary poles, but there is flux reversal when motor commutates from one phase to the next phase. This flux reversal will increase the core losses in the motor. Therefore, to select the suitable winding polarity for rated operation, further analysis has been done in this paper.

Fig. 8 shows the variation of the magnetic flux density in the different parts of the DSSRM at rated speed. To measure the flux density in the different part of the 12/10 pole DSSRM, the mid-point or center point of the respective parts are considered which is shown in Fig. 8 (a). It can be seen that the flux density waveforms are periodic and non-sinusoidal in the different parts of the motor. The frequency of the flux waveforms in the exciting pole, auxiliary pole and stator yoke is 100 Hz, while in rotor segments it is 60 Hz and 30 Hz for aiding and subtracting flux winding polarities, respectively. Therefore, determining the sinusoidal components of these loss-causing flux density waveforms is essential [34]. Table 4 deals with this data. It can be observed in Fig. 8 (b) and Fig. 8 (d) that the flux reversal in the exciting pole and stator yoke of the machine is absent. Also, the machine with aiding flux winding polarity has a higher dc component in the auxiliary pole. However, in the case of subtracting flux
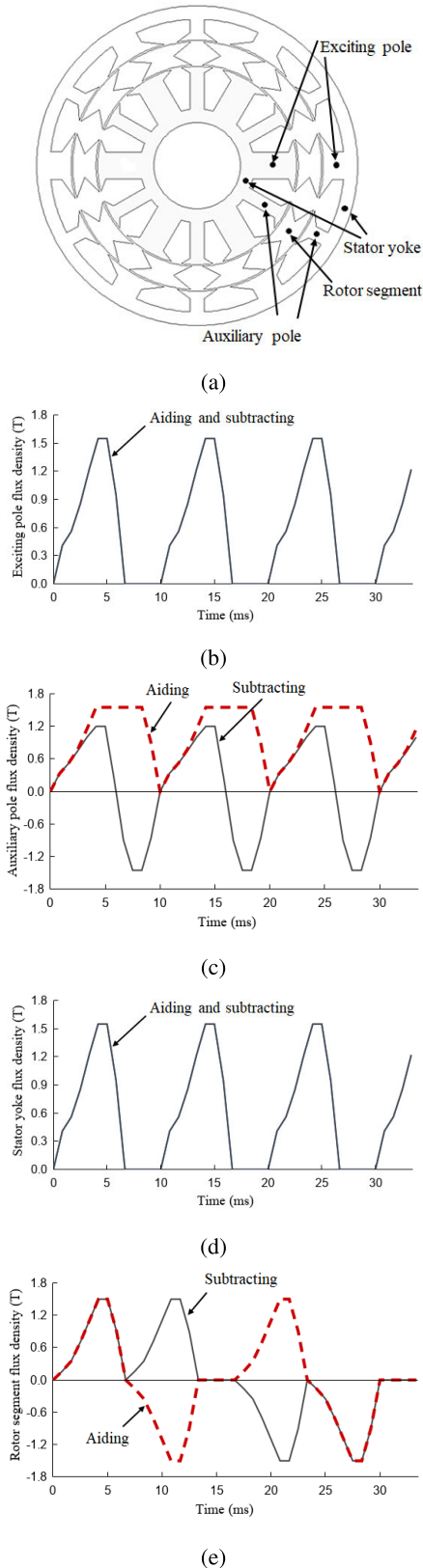
(a)

(b)

(c)

(d)

(e)

FIGURE 8. Flux density variation in different parts of DSSRM.
(a) Geometry points for flux density calculation. (b) Exciting pole.
(c) Auxiliary pole. (d) Stator yoke. (e) Rotor segment.

TABLE 4. Magnitude of the different harmonics of flux densities in different part of DSSRM.

Harm. order	Flux density (T)							
	Exc. pole		Aux. pole		Stator yoke		Rotor segment	
	W1	W2	W1	W2	W1	W2	W1	W2
DC	0.59	0.59	1.08	0.05	0.59	0.59	0	0
1	0.78	0.78	070	1.24	0.78	0.78	1.05	0.98
2	0.24	0.24	0.24	0.46	0.24	0.24	0.45	0
3	0.15	0.15	0.16	0.03	0.15	0.15	0.25	0.29
4	0.07	0.07	0.11	0.08	0.07	0.07	0.22	0
5	0.03	0.03	0.05	0.01	0.03	0.03	0	0.59

W1- aiding flux winding polarity, W2- subtracting flux winding polarity

TABLE 5. Comparison between aiding and subtracting flux winding polarities.

Parameter	Aiding flux	Subtracting flux
Torque T_{avg} in N-m	40.0	40.1
Axial length (l) in mm	87.5	86
Core loss in W	50	53
Iron weight in kg	11.96	11.75
Copper weight in kg	2.81	2.78
Total active weight in kg	14.77	14.53

winding polarity, flux reversal exists as shown in Fig. 8 (c), which eventually increases the core losses. The performance comparison of the DSSRM with aiding and subtracting flux winding polarities for the rated output torque is made and the results are listed in Table 5. It is observed that the aiding flux winding polarity has slightly lower core losses, however, for the rated output torque, it requires higher axial length and active weight as compared to the subtracting flux winding polarity. It is also observed that there is a less margin to differentiate between the performance of these polarities to make a versatile conclusion on these. The result may be affected as per the machine's operating condition, for instance, change in operating speed, change in a material property of the core. However, as per the considered operating condition and rated speed, subtracting flux winding polarity is considered for further analysis in this paper.

VI. TORQUE RIPPLE REDUCTION THROUGH ROTOR SEGMENTS SHIFT

The main region of torque ripple generation in SRMs is during the commutation of the outgoing phase. During this period, the torque shared by the outgoing phase reduces significantly. However, at the same time, the value of $dL/d\theta$ is less for the incoming phase. Because of this, the torque generated by the incoming phase is less in this region. This phenomenon results in a large torque dip and subsequently large torque ripples in this region. Fig. 9 shows the pictorial representation of this phenomenon. Fig. 9 (a) shows the typical torque profiles of two consecutive phases; phase A and phase B (solid lines) which are separated by the stroke angle θ_{stk}. At the start of the commutation of phase A, the torque contributed by this phase becomes negligible.
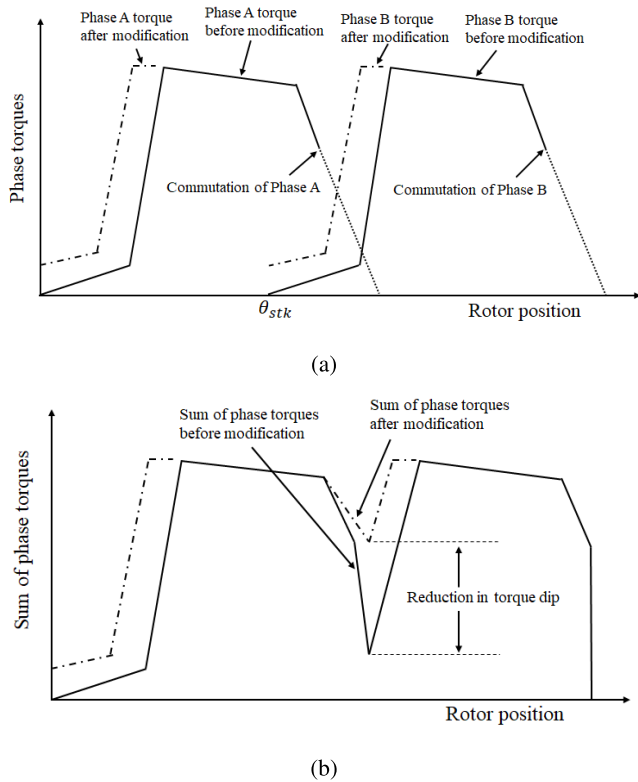
(a)

(b)

FIGURE 9. Schematic for torque ripple reduction. (a) Phase torques. (b) Sum of phase torques.
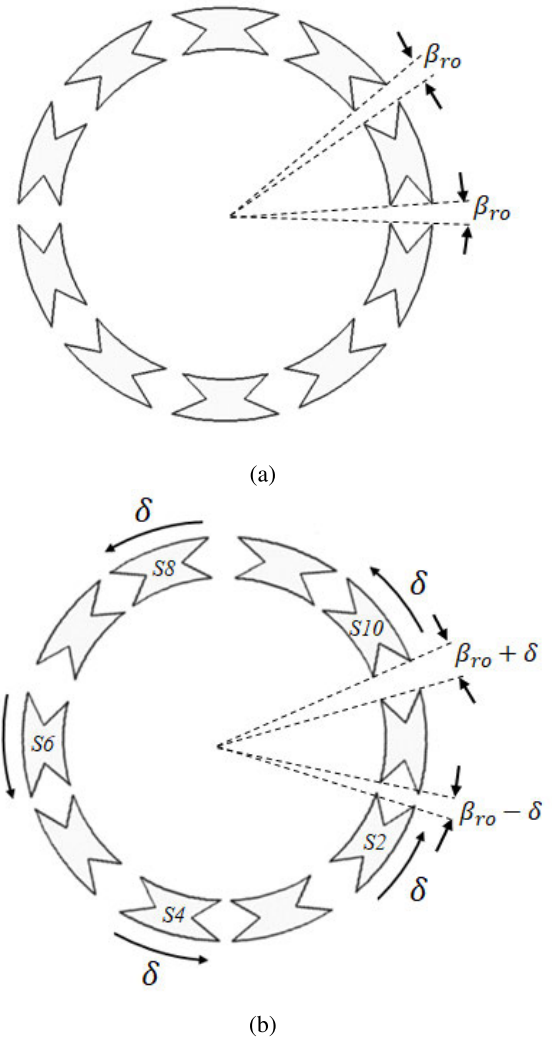

(a)

(b)

FIGURE 10. Proposed design modification in rotor. (a) Rotor without segments shift (before modification). (b) Rotor with segments shift (after modification).

At the same time, phase B does not achieve sufficient torque generation. Fig. 9 (b) shows the sum of these torques (solid line) with the consideration of the commutation effect. It is seen that a large torque dip occurs in this region which results in a high torque ripple in the motor. However, if the structural modification is accomplished in the machine in such a way that the incoming phase has increased torque in this region, the torque dip will reduce, which subsequently will reduce the torque ripple. The figures of the proposed phase torques and sum of the phase torques after modification are represented in Fig. 9 (a) and Fig. 9 (b), respectively, with dot-dash lines. It can be seen that in the case of a modified structure if the incoming phase has increased torque generation, the torque dip can reduce which can further reduce the torque ripple.

In [26], various methods of PM grouping and shifting techniques are discussed to reduce the torque ripple due to the cogging effect for AFPM motor. In this study, the angular shift of rotor segments is analysed to reduce the torque ripple in DSSRM. In FEM based simulation study, it is observed that shifting of all the rotor segments does not provide a significant reduction in the torque ripple. Therefore, shifting of the alternate rotor segments with an angle of δ in the direction of rotation is discussed here. This design modification is implemented in the rotor of DSSRM which is illustrated in Fig 10. Fig. 10 (a) highlights the placement of the rotor segments in case of an original motor in which the adjacent rotor segments have uniform separation of β_{ro}
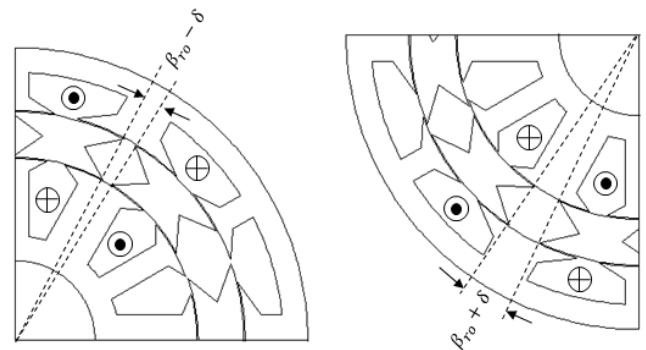

FIGURE 11. Structure of DSSRM after segments shift with respect to consecutive exciting poles of a phase.

between them. In the proposed motor, the alternate rotor segments viz. S2, S4, S6, S8 and S10 are shifted in the direction of rotation with an angle δ from their original position as shown in Fig. 10 (b). Fig. 11 shows the structure of the

proposed DSSRM after segments shift with respect to the exciting poles of the motor. It is seen that for two consecutive exciting poles of a phase, the separation between the adjacent rotor segments is decreased and increased respectively. Therefore, the proposed design modification is only valid for the machines with even multiplicity ($m = 2, 4, \ldots$ etc.) with the number of rotor segments $N_r = m(4n \pm 1)$; where n is a positive integer number. For the slot/segments combinations as discussed in Section IV, this design modification is only valid with 12/10 and 12/14 pole combinations. It has been already observed that the 12/10 pole combination has better performance over 12/14 pole machine and has already been considered for the analysis in this paper. In the case of proposed DSSRM with the segments shift, the inductance profile is modified and the value of $dL/d\theta$ increases for the incoming phase. This increases the torque shared by the incoming phase in the commutation region which reduces torque dip and torque ripple in this region.

TABLE 6. 12/10 pole DSSRM design specifications.

Parameter	Value
Outer and inner diameters (D_o, D_i)	200 mm, 54 mm
Average diameter of rotor (D_r)	140.5 mm
Axial length (l)	86 mm
Stator yoke iron width	8.5 mm
Stator slot opening angle (β_{so})	6°
Arc angle of exciting and auxiliary poles (β_{exc}, β_{aux})	30°, 18°
Rotor segments arc angle and separation angle (β_r, β_{ro})	30°, 6°
Inner and outer air-gap length (l_g)	0.4 mm
Number of conductors per slot	54
Phase resistance	0.471 Ω
Rated DC link voltage	170 V
Peak phase current	26 A

VII. FINITE ELEMENT MODELING AND SIMULATION RESULTS

Table 2 and Table 6 gives the details of the design specifications of the 3-phase 12/10 pole DSSRM. The 2-D FEM simulation model is established in ANSYS/MAXWELL software to obtain the electromagnetic performance of the DSSRM. The basic steps followed for the analysis are modelling, assigning material properties, assigning boundaries, meshing, providing excitation and analysis set-up and finally, the response is simulated. The basic governing equations used for simulation are Maxwell's equations. Backward Euler solver is used in this analysis. The core material selected for stator and rotor is 'steel-1008' which is imported from the software library. To calculate the core losses 0.4 mm thickness of laminations is considered. In meshing, triangular mesh elements of maximum 2 mm size for stator and rotor core material and 1 mm for copper material are considered. The zero vector potential boundary is considered at the outer surface of the model so that the flux does not move outside of this surface. To obtain the dynamic response of the machine, a conventional 3-phase asymmetric half-bridge converter is used. The phase conduction period considered for each phase is between 0°-14.5° (mech.). To maintain the phase currents, hysteresis current control is used with the hysteresis band of

$\pm$ 0.4 A and the reference current of 26 A. To calculate the torque ripple and the efficiency of the motor, Eq. (20) and (21) are used, respectively.

$$T_{ripple} = (T_{max} - T_{min})/T_{avg} \qquad (20)$$

$$\eta = P/(P + P_{Fe} + P_{Cu}) \qquad (21)$$

where T_{max}, T_{min} and T_{avg} are the maximum, minimum and average value of the output torque respectively. η, P_{Fe} and P_{Cu} are the efficiency, iron loss and copper loss respectively, and P is the total output power without mechanical loss.
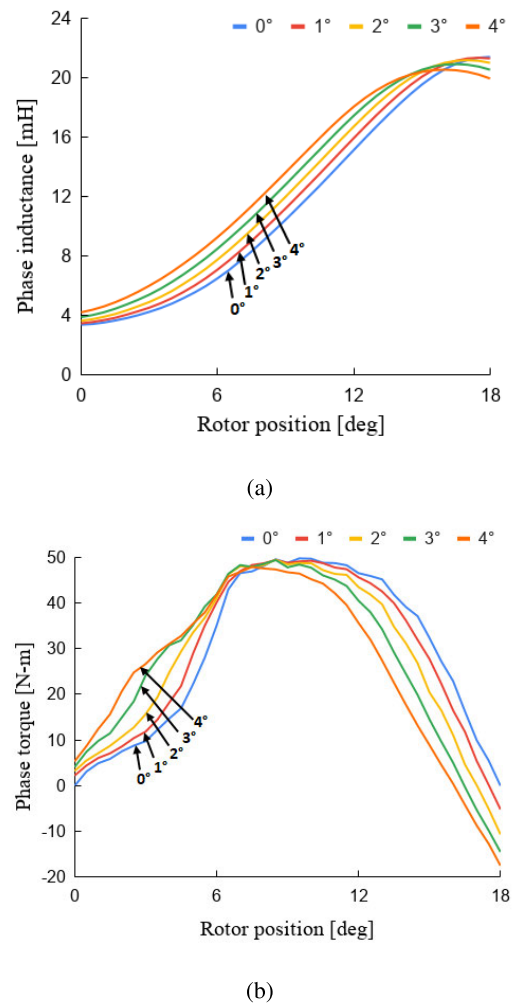

(a)

(b)

FIGURE 12. Static inductance and static torque profiles with variation of segments shift angle (δ). (a) Static inductance. (b) Static torque.

A. INFLUENCE OF ROTOR SEGMENTS SHIFT ON STATIC INDUCTANCE AND TORQUE PROFILES

Fig. 12 shows the static inductance and static torque profiles of the DSSRM for rated current with the segments shift angle δ between 1°- 4°. It is observed in Fig. 12 (a) that the value of unaligned inductance and the value of $dL/d\theta$ increase near the unaligned position (here in this case 0° rotor position) with the increase in δ. However, the value of aligned

inductance and the value of $dL/d\theta$ reduces near aligned position (here in this case 18° rotor position) with the increase in δ. In Fig. 12 (b), it is observed that the phase torque of the machine increases near the unaligned position with the increase in δ. However, with the increase in δ, the phase torque also reduces near the aligned rotor position because of the decrease in $dL/d\theta$ in this region.
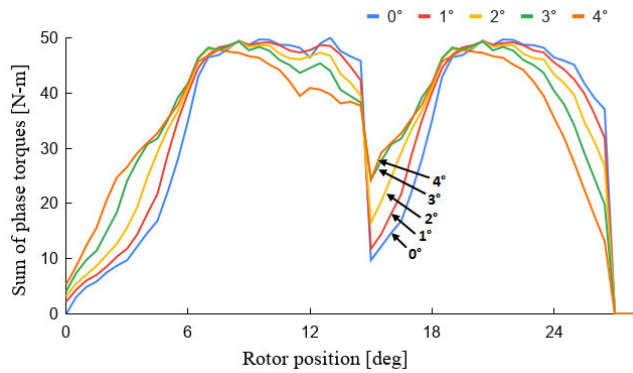

FIGURE 13. Sum of the static phase torques with the shift of the rotor segments showing reduction in torque dip in commutation region.

Fig. 13 shows the sum of the static phase torques of phase A and phase B which are separated by the stroke angle (12° in this case) for the value of δ between 1°-4° considering the commutation effect. The phase commutation angle taken is 14.5° (mech). It is assumed that after the commutation of the outgoing phase, the torque contributed by that phase becomes negligible. It is seen in the figure that with the increase in δ between 1°-3°, the torque dip occurring in the commutation region reduces. This is because the torque of the incoming phase increases with the increase in δ, consequently, the sum of phase torques increases. However, it is also observed that for $\delta = 4°$ the torque dip becomes more as compared to $\delta = 3°$. This is because in this case the reduction in torque of the outgoing phase near aligned rotor position becomes more dominant over the increase in the torque of incoming phase and subsequently, the sum of phase torques reduces. Therefore, it can be concluded that the value of δ for minimum torque dip and minimum torque ripple lies between 2°-4°. To obtain the condition of minimum torque ripple and the value of δ for this, the dynamic response of the proposed machine is further analysed through FEM in the next subsection.

B. DYNAMIC RESPONSE AND ANALYSIS OF TORQUE RIPPLE REDUCTION

The dynamic response of the DSSRM is obtained through FEM based simulation analysis for the value of δ between 0°-4°. The variation in the output torque and torque ripple with the variation δ is shown in Fig. 14 for rated speed. The output torque and torque ripple for the DSSRM without segments shift ($\delta = 0°$) are 40.1 N-m and 78.5% respectively. With the shift of the rotor segments, the torque ripple starts decreasing. The minimum value of torque ripple is obtained
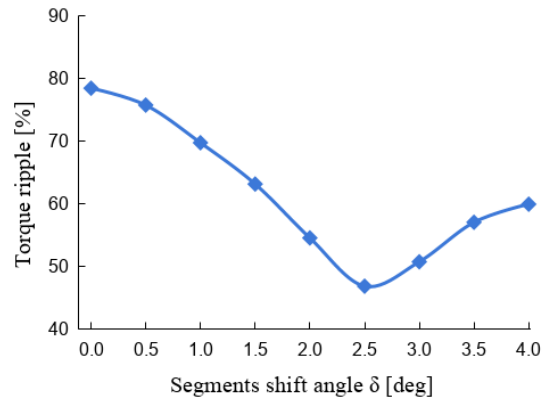
(a)
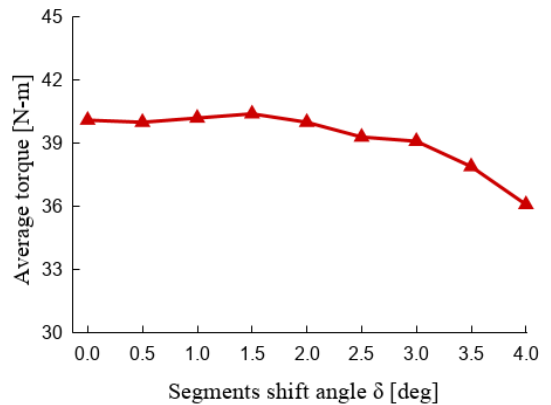
(b)

FIGURE 14. Variation of torque ripple and average output torque with rotor segments shift angle δ. (a) Torque ripple. (b) Average torque.

for the shift angle δ of 2.5°. The torque ripple, in this case, is 46.8% with an output torque of 39.3 N-m. Consequently, the torque ripple reduces by nearly 40%, however, the output torque also reduces by 2%. For the further increase in δ, the torque ripple starts increasing and the output torque also reduces considerably. Therefore, the optimal value of δ for the proposed machine is 2.5°.

Fig. 15 shows the flux density plot of the half section of the FEM model of DSSRM in unaligned and aligned rotor positions, respectively for $\delta = 2.5°$. The peak MMF considered is 1404 AT per slot. Fig. 16 and Fig. 17 show the dynamic variation of phase currents and output torque for the DSSRM without and with rotor segments shift, respectively, at the rated speed. To obtain the dynamic performance, the phase current overlap technique is used to increase the output torque and to reduce the torque ripple [35] in both cases. From Fig. 16 (b), the average torque, peak-to-peak torque ripple and % torque ripple is found to be 40.1 N-m, 31.5 N-m and 78.5%, respectively, for the DSSRM without segments shift. The above values change to 39.3 N-m, 18.4 N-m and 46.8% respectively for the DSSRM with segments shift ($\delta = 2.5°$) as shown in Fig. 17 (b). Table 7 compares the performance data of these. It is seen that the torque ripple is reduced

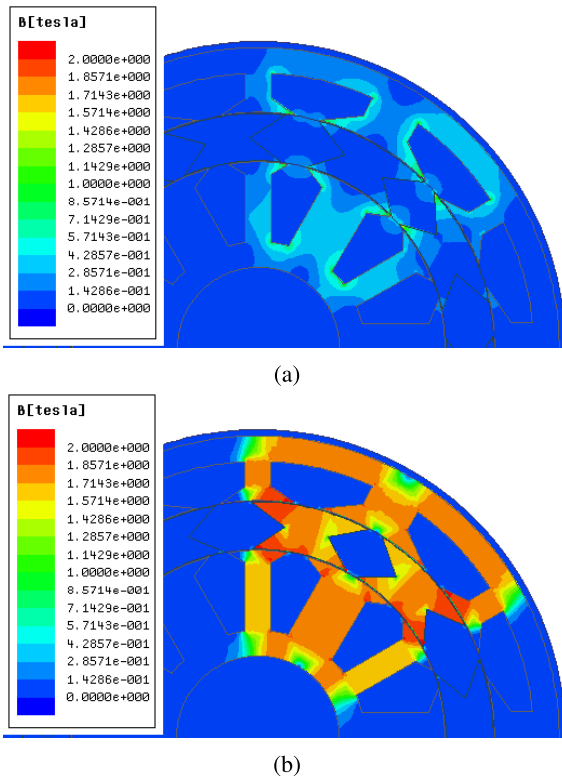**FIGURE 15.** Flux density plot of the FEM model of DSSRM with rotor segments shift ($\delta = 2.5°$). (a) Unaligned position. (b) Aligned position.

FIGURE 16. Phase currents and torque variation with rotor position for DSSRM without segments shift. (a) Phase currents. (b) Dynamic torque.

TABLE 7. Performance comparison of DSSRM without and with rotor segments shift.

Parameter	Without segment shift ($\delta = 0°$)	With segments shift ($\delta = 2.5°$)
Output torque	40.1 N-m	39.3 N-m
Peak-to-peak torque riple	31.5 N-m	18.4 N-m
Torque ripple	78.5%	46.8%
Unaligned inductance	3.53 mH	3.77 mH
Aligned inductance	21.85 mH	21.07 mH
Reduction in torque ripple	-	40%
Reduction in output torque	-	2%
Core loss	53 W	60 W
Copper loss	362 W	362 W
Rated efficiency	85.8%	85.4%

by 40% with the shift of rotor segments by 2.5°. However, the output torque is also reduced by 2%. The rated efficiency of the proposed machine is 85.4%, which is comparable with the baseline machine. The total active weight of the proposed DSSRM is 14.53 kg with torque to active weight ratio of 2.70 N-m/kg. Fig. 18 compares the dynamic torque of the DSSRMs without and with the rotor segments shift. It is seen that the torque dip occurring in the commutation region reduces in the case of the proposed motor and therefore, the torque ripple decreases. Fig. 19 shows the simulated torque-speed characteristics for the proposed DSSRM. It is observed that the machine has nearly flat torque profile till the rated speed which is one of the primary requirements in
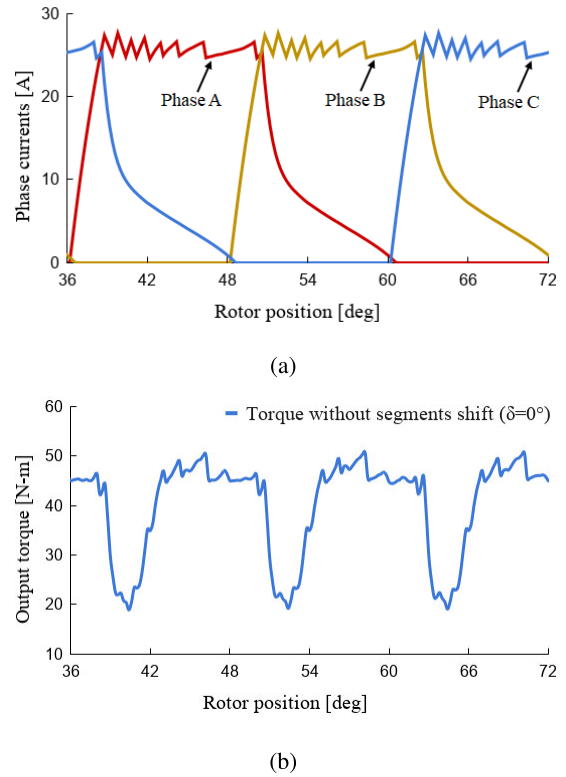
direct drive electric vehicles. Therefore, this machine can be regarded as a suitable candidate for such applications.

## C. HARMONIC ANALYSIS OF TORQUE RIPPLE FREQUENCIES

The torque dip and torque ripple are reduced in the case of DSSRM with the alternate rotor segments shift which can be observed in Fig 18. The harmonics spectrum of various frequencies of the dynamic output torque without and with rotor segments shift is shown in Fig. 20. The average or DC value of the output torques are 40.1 N-m and 39.3 N-m, respectively, without and with rotor segments shift which are same as in the previous subsection. The fundamental frequency of torque ripple for both the machines is 300 Hz (as shown in Fig. 18) which is the most dominant harmonic also in this case. The magnitude of this harmonic is 28.5% and 19.8% of the output torque without and with the rotor segments shift, respectively. Therefore, there is an 8.7% reduction in fundamental torque ripple in the proposed motor. For the second harmonic, these values are 16.3% and 4.7%, respectively, which shows an 11.6% reduction for this harmonic. It is observed that the low-frequency torque ripples are reduced in the case of shifted rotor motor.

D. SUITABILITY FOR REVERSE MOTORING

Because of the symmetrical structure of the rotor with respect to the CCW and CW orientations, the proposed motor is also
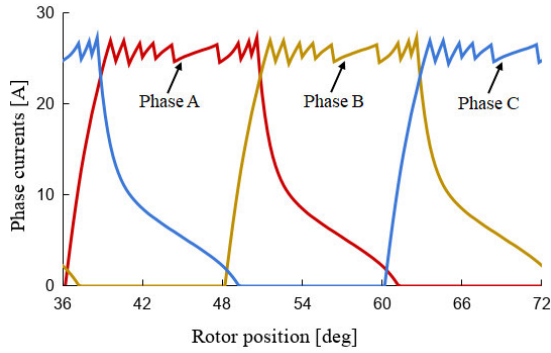
(a)
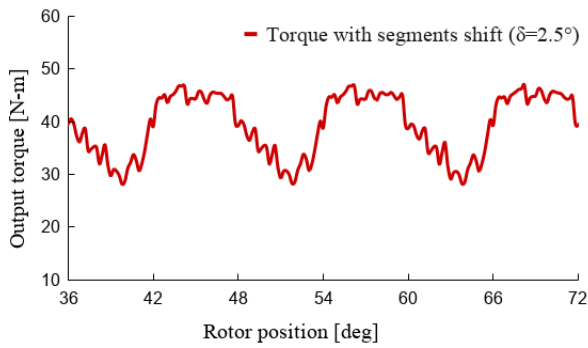
(b)

FIGURE 17. Phase currents and torque variation with rotor position for DSSRM with segments shift (δ = 2.5°). (a) Phase currents. (b) Dynamic torque.
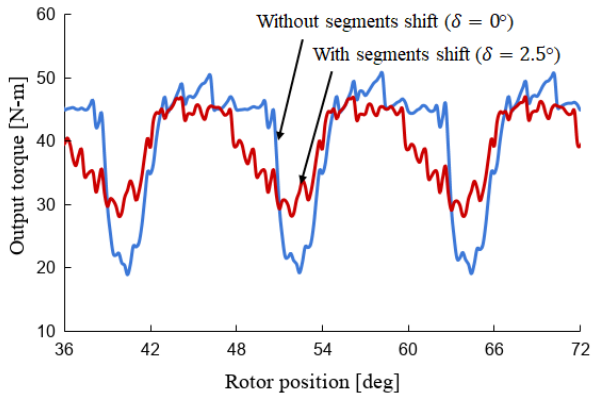

FIGURE 18. Comparison of dynamic torques showing the reduction in torque dip in commutation region in proposed DSSRM.

suitable to reduce the torque ripple for the reverse direction of rotation. However, in the case of reverse motoring, the definition of 0° rotor position for the proposed motor changes to ($36° \times n - 2.5°$) of the forward motoring, where *n* is a positive integer number. The performance of the proposed motor is simulated through FEM for the reverse direction of rotation at rated speed and the results are given in Table 8. In this case, the output torque and torque ripple for the proposed motor is
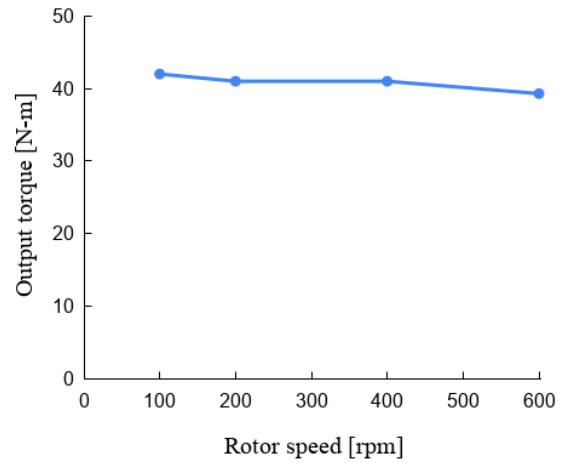

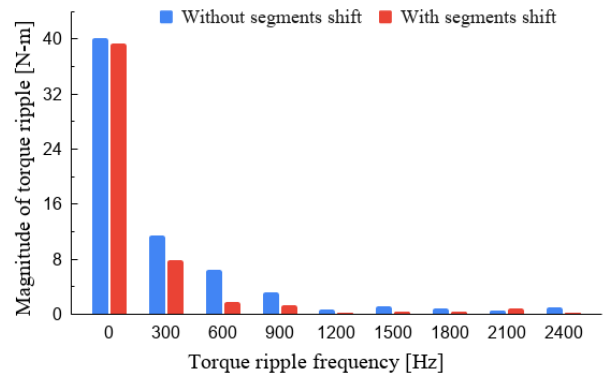**FIGURE 19.** Variation of output torque with rotor speed.

FIGURE 20. Comparison of torque ripple harmonics showing the reduction in lower order torque harmonics in proposed DSSRM.

TABLE 8. Performance data for reverse motoring.

Parameter	Without segment shift ($\delta = 0°$)	With segments shift ($\delta = 2.5°$)
Output torque	40.0 N-m	39.3 N-m
Peak-to-peak torque riple	31.4 N-m	18.5 N-m
Torque ripple	78.5%	47.1%
Reduction in torque ripple	-	40%
Reduction in output torque	-	2%
Core loss	53 W	60 W
Copper loss	362 W	363 W
Rated efficiency	85.8%	85.4%

39.3 N-m and 47.3%, respectively, with approximately 40% reduction in torque ripple. These values are nearly the same as in the case of forward motoring for the same motor (as given in Table 7). The losses and rated efficiency are also comparable in both the cases i.e. for CCW and CW rotations.

E. VARIATION IN FLUX DISTRIBUTION AND ITS AFFECTS
In this subsection, the effect of the segments shifts on the flux distribution in the rotor segments as well as air-gaps is analysed and discussed. Fig. 21 (a) shows the variation in the maximum flux density occurring in the rotor segments with δ. The shifting of the rotor segments results the adjacent rotor segments becoming closer, therefore, the leakage flux
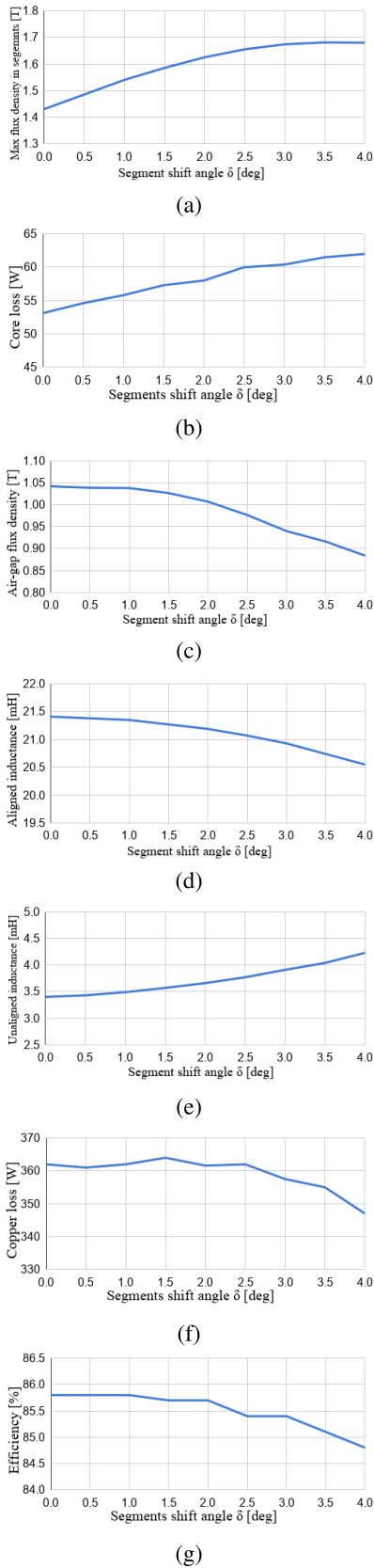
FIGURE 21. Variation in the parameters of DSSRM with δ. (a) Variation in flux density in segments. (b) Variation in core loss. (c) Variation in air-gap flux density. (d) Variation in aligned inductance. (e) Variation in unaligned inductance. (f) Variation in copper loss. (g) Variation in efficiency.

increases in these segments. This increases the maximum flux density in the rotor segments. As shown in the figure, the maximum flux density in the segments is 1.43 T for δ = 0° which increases to 1.65 T for δ = 2.5°. With further increase in δ, the saturation effect becomes more significant and flux density becomes nearly constant in the rotor segments. With the increase in flux density, the core loss increases. Fig. 21 (b) shows the variation in core loss of motor with δ. The core loss increases with the increase in δ because of the increase in the flux density in rotor segments.

Fig. 21 (c) shows the variation in air-gap flux density with δ. The air-gap flux density shown is the average value of inner and outer air-gaps. With the increase in δ, the air-gap flux density near an excited rotor segment decreases. It is seen that the decrease in air-gap flux density is more rapid for δ greater than 2°. As it is seen in Eq. (4), the aligned inductance is directly dependent on the air-gap flux density and it also decreases with the increase in δ, as shown in Fig. 21 (d). Fig. 21 (e) show variation in the unaligned inductance with δ. It is seen that with the increase in δ, the unaligned inductance increases. This is because, with the increase in δ, the leakage flux in the rotor segments increases at the unaligned condition. As given in Eq. (8), the decrease in air-gap flux density and aligned inductance, and the increase in unaligned inductance will result in the reduction of the output torque for the higher value of δ. In Fig. 14 (b), it can be observed that the output torque reduces more rapidly for δ above 2.5°. The increase in unaligned inductance further reduces the rate of increase of the phase currents. Therefore, the RMS value of phase current and the copper loss starts decreasing above the value of δ = 2.5°, as shown in Fig. 21 (f). However, the decrease in phase current will further reduce the output torque and power.

It is observed that for the higher values of δ, above 2.5°, the decrease in air-gap flux density and aligned inductance; and increase in unaligned inductance is significant which will reduce the phase current and output torque. The reduction in torque and power leads to the reduction in efficiency as shown in Fig. 21 (g).

The electromagnetic forces in an electric machine results due to the interaction between normal and tangential components of air-gap flux density. The tangential and radial force densities in the air-gap can be expressed as [23]

$$f_t = \frac{1}{2\mu_0} 2B_n B_t \tag{22}$$

$$f_r = \frac{1}{2\mu_0}(B_n^2 - B_t^2) \tag{23}$$

where f_t and f_r are the tangential and radial force densities in air-gap, respectively; B_n and B_t are the normal and tangential components of air-gap flux density, respectively. The tangential force density, f_t is responsible for the generation of torque in the machine, while radial force density, f_r leads to the generation of radial force and mechanical vibration in the machine.
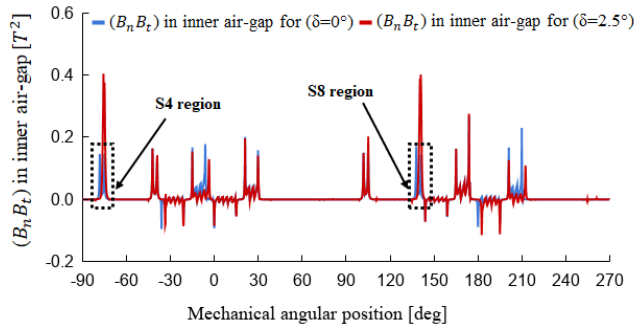
(a)
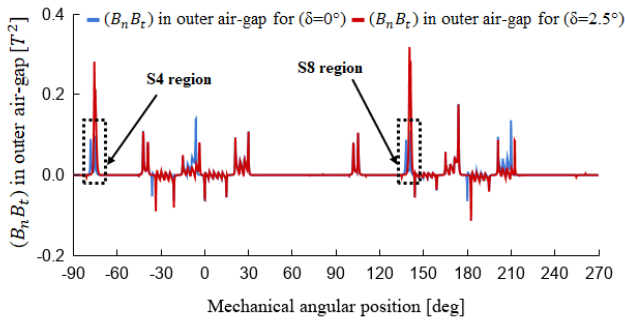
(b)

FIGURE 22. Variation of (B_nB_t) in inner and outer air-gaps of 12/10 pole DSSRM just after the start of commutation of phase A. (a) Inner air-gap. (b) Outer air-gap.

The value of (B_nB_t) in inner air-gap of the 12/10 pole DSSRM is shown in Fig. 22 (a), without and with rotor segments shift between -90° to 270° mechanical position of motor (referred from Fig. 2 (a)). This value is shown in Fig. 22 (b) for outer air-gap. The rotor position considered is 15° (mech.), just after the start of the commutation of phase A. With the excitation of phase B, the segment S3, S4, S8 and S9 go into its magnetic influence. It is seen in Fig. 22 (a) and Fig. 22 (b) that the value of (B_nB_t) in the inner and outer air-gaps, near the segments S4 and S8 region, is increased in the case of shifted segments. Therefore, more tangential forces are exerted on these segments which increase the torque of the motor in the commutation region. Because of this, the torque dip and subsequently, the torque ripple reduces in this region.

F. EFFECT OF SEGMENTS SHIFT ON RADIAL FORCE AND VIBRATION

It is seen in Eq. (23) that the radial force density is directly dependent on the value of $(B_n^2 - B_t^2)$ in the air-gap. In Fig. 23, the value of $(B_n^2 - B_t^2)$ in the inner and outer air-gaps of the 12/10 pole DSSRM for $\delta = 0°$ is shown between -90° to 270° mechanical position of motor (referred from Fig. 2 (a)). The rotor position considered is 90° (elec.) with phase A excited with the rated current. It is seen in the figure that the air-gaps near the S1, S2, S6 and S7 segments region have
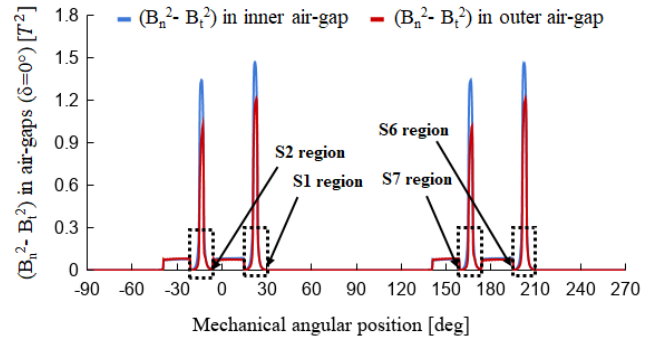

FIGURE 23. Variation in $(B_n^2 - B_t^2)$ in the inner and outer air-gaps of 12/10 pole DSSRM for $\delta = 0°$ with 90° (elec.) rotor position.

higher value of $(B_n^2 - B_t^2)$ in the inner and outer air-gaps. The values are greater in the inner air-gap as compared to the outer air-gap for the respective segments. Therefore, resultant attractive radial forces are created on the segments towards the inner stator direction. The average values of $(B_n^2 - B_t^2)$ are calculated between -90° to 90° for the inner and outer air-gaps of the motor which have the values of 0.0665 T^2 and 0.0528 T^2 respectively. These value for 90° to 270° position range are 0.0665 T^2 and 0.0527 T^2 respectively. The difference between these pair of values is approximately the same. Therefore, it is concluded that the segments S1 and S6 bear the same but opposite radial force towards inner stator direction. Similarly, S2 and S7 bear the same but opposite radial force towards inner stator direction. Because of these equal and opposite forces, the rotor has a balance condition and have the least vibration for $\delta = 0°$. Fig. 24 shows the static radial force working on segments S1, S2, S6 and S7 between 0°-18° rotor position with phase A excited with the rated current. It is seen that the magnitude of the attractive radial forces on S1 and S6 is the same, similarly, it is same for S2 and S6.
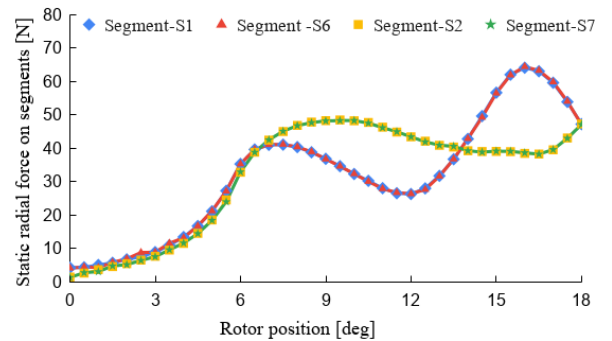

FIGURE 24. Static radial force on the segments of 12/10 pole DSSRM for $\delta = 0°$ with phase A excitation.

With the shift of rotor segments, the angular separation between S1 and S2 reduces, whereas for S6 and S7 it increases. Fig.25 shows the variation in the value of $(B_n^2 - B_t^2)$ in the inner and outer air-gaps of the 12/10 pole DSSRM for $\delta = 2.5°$. It is observed that the difference in
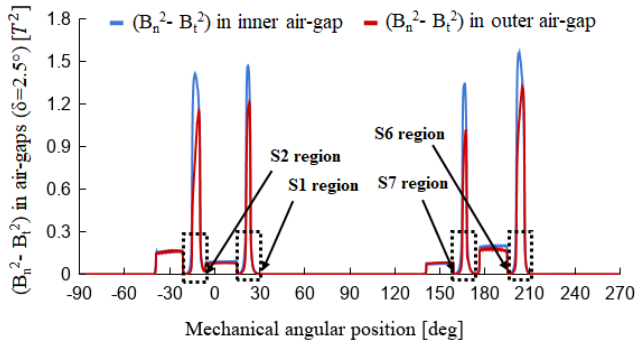
FIGURE 25. Variation in $(B_n^2 - B_t^2)$ in the inner and outer air-gaps of 12/10 pole DSSRM for $\delta = 2.5°$ with 90° (elec.) rotor position.
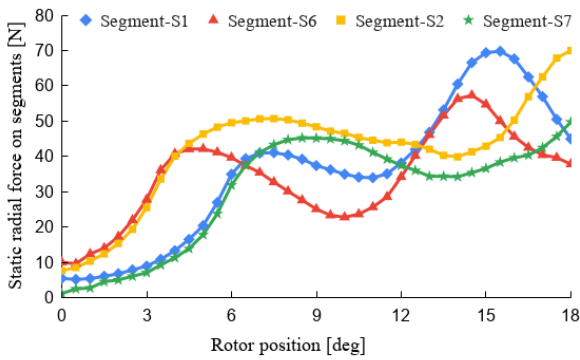

FIGURE 26. Static radial force on the segments of 12/10 pole DSSRM for $\delta = 2.5°$ with phase A excitation.
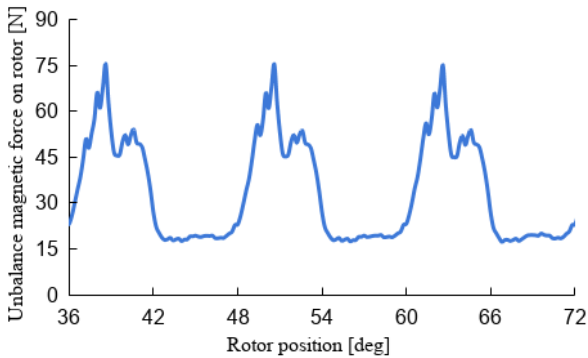

FIGURE 27. Dynamic unbalanced magnetic force on the rotor of 12/10 pole DSSRM with $\delta = 2.5°$.

$(B_n^2 - B_t^2)$ for inner and outer air-gaps increases in the region of S1 and S2 as compared to the region of S6 and S7. Therefore, S1 and S2 bear higher radial forces as compared to S6 and S7. Because of the unequal forces on the segments of the opposite sides of the rotor, a resultant force is created on it. Fig. 26 shows the static radial force working on segments S1, S2, S6 and S7 between 0°-18° rotor position with phase A excited with the rated current for $\delta = 2.5°$. It is seen that the magnitude of the attractive radial forces on S1 and S6 are not same, similarly, it is not same for S2 and S7. Fig. 27 shows the dynamic variation of the unbalanced magnetic force on the

rotor for $\delta = 2.5°$ in the case of rated operating condition. The average value of the unbalanced force on the rotor for $\delta = 0°$ is negligible and has a value of 0.7 N. However, a small unbalanced force exists on the rotor of an average value of 33.9 N for $\delta = 2.5°$. The average value of this unbalance force per cm of axial length is 3.94 N/cm. This small value will not cause any bending effect on the shaft, however, this force will lead some increase in mechanical vibrations in the motor.
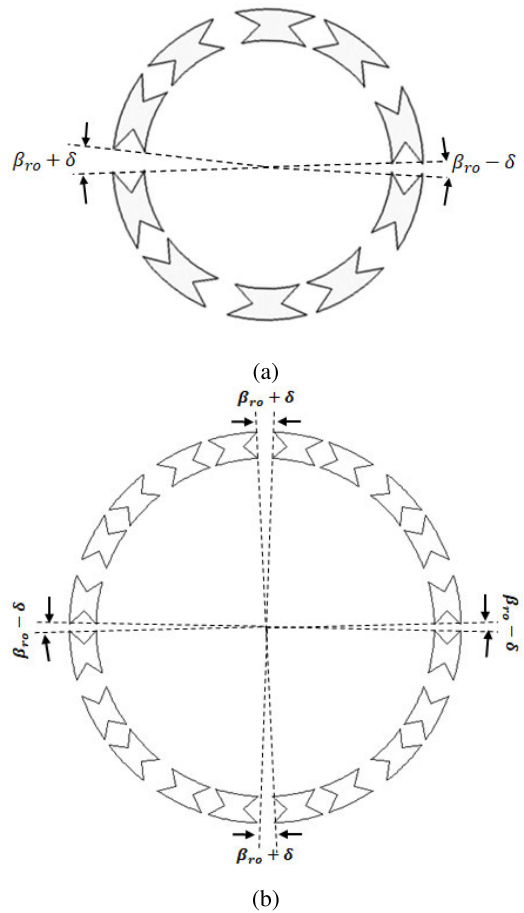

FIGURE 28. Structure of the rotor of 12/10 and 24/20 pole DSSRM with shifted segments. (a) 12/10 pole DSSRM. (b) 24/20 pole DSSRM.

The unbalanced magnetic force created on the rotor of a 12/10 pole DSSRM is primarily caused by the unequal non-magnetic separation between the adjacent rotor segments at opposite sides of the rotor, as shown in Fig. 28 (a). This creates unequal radial force densities at opposite sides of the rotor. In the case of a 24/20 pole DSSRM, the number of stator and rotor poles becomes twice. Unlike 12/10 pole DSSRM, in 24/20 pole DSSRM, the non-magnetic separation between adjacent rotor segments becomes same at the opposite sides of the rotor, as shown in Fig. 28 (b). Because of this, the radial force densities in the air-gaps of opposite sides of the rotor become equal. This inherently omits the problem of unbalanced condition on the rotor and reduces the mechanical vibration in the motor. Fig. 29 shows the variation of output
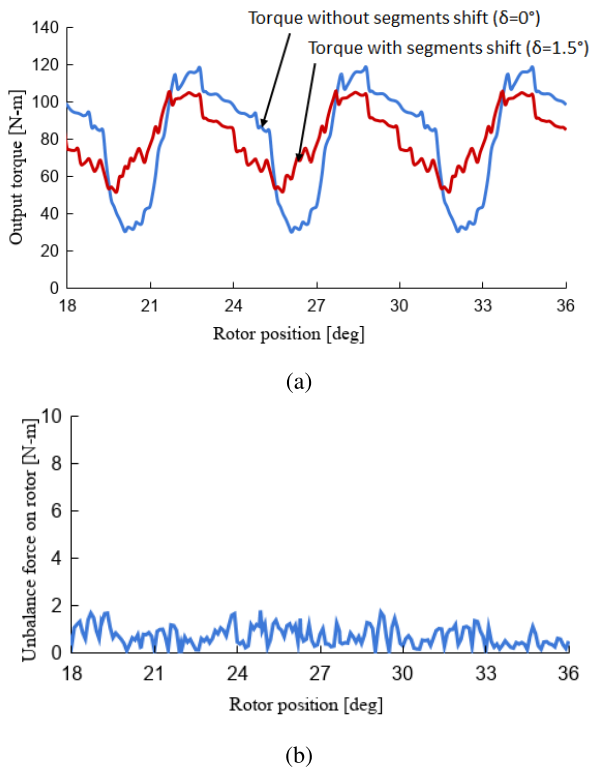
(a)

(b)

FIGURE 29. Dynamic torque and force profiles for 24/20 pole DSSRM. (a) Dynamic torque. (b) Unbalance magnetic force on rotor with $\delta = 1.5°$.

TABLE 9. 24/20 pole DSSRM design parameters.

Parameter	Value
Outer diameters (D_o)	292 mm
Average diameter of rotor (D_r)	229.5 mm
Axial length (l)	86 mm
Stator yoke iron width	8.4 mm
Stator slot opening angle (β_{so})	3.5°
Arc angle of exciting and auxiliary poles (β_{exc}, β_{aux})	14.5°, 8.5°
Rotor segments arc angle and separation angle (β_r, β_{ro})	14.5°, 3.5°
Inner and outer air-gap length (l_g)	0.4 mm
Number of conductors per slot	42
Peak phase current	23 A

TABLE 10. Performance data for 24/20 pole DSSRM without and with rotor segments shift.

Parameter	Without segment shift ($\delta = 0°$)	With segments shift ($\delta = 1.5°$)
Rated speed	600 rpm	600 rpm
Output torque	81.3 N-m	80.2 N-m
Torque ripple	108.4%	65.9%
Reduction in torque ripple	-	39.2%
Reduction in output torque	-	1.4%
Unbalance force on rotor	0.6 N	0.5 N
Core loss	297 W	334 W
Copper loss	394 W	396 W
Rated efficiency	88.0%	87.3%

torque without and with rotor segments shift and the dynamic unbalance force on the rotor for a 3-phase, 5 kW, 24/20 pole DSSRM. In the case of shifted segments, the % reduction in torque ripple is 39.2% and the unbalanced force on the rotor is 0.5 N which is negligible. Table 9 and Table 10 contains the design and performance data for this motor.

VIII. CONCLUSION

In this paper, several design procedures to improve the performance of the radial flux DSSRM with single-tooth winding topology are discussed. Firstly, the equations of the stator and rotor pole arc angles for low unaligned and high aligned inductances for high output torque are derived and based on this, the selection of the number of stator slots/rotor segments is analysed. It is observed that for 3-phase DSSRM, 12/10 pole combination has better torque density over 12/8 and 12/14 pole combinations. In 12/10 pole combination, higher torque is achieved as compared to 12/8 pole combination because of the higher number of strokes per revolution; however, in 12/14 pole combination, the benefit of the higher number of strokes per revolution becomes ineffective because of the significant increase in unaligned inductance. Furthermore, the influence of winding polarities on the performance of DSSRM is investigated. It is observed that unlike subtracting flux winding polarity, aiding flux winding polarity has no flux reversal in auxiliary poles; therefore, it has lower core loss. However, it has lower torque density as compared to subtracting flux winding polarity because of saturation in auxiliary poles. As per the considered operating condition, subtracting flux winding polarity is considered in this paper. Finally, the design modification in the rotor structure is proposed with the angular shift in the alternate rotor segments in the direction of rotation to mitigate the torque ripple. A detailed analysis of the proposed technique is carried out for the 3-phase 12/10/12 pole DSSRM. A FEM based model is developed and simulated in order to investigate the effectiveness of the proposed design. It is observed that with this design modification, the torque generating capability of the incoming phase increases, which reduces the torque dip in the commutation region. Subsequently, the torque ripple is reduced by nearly 40% as compared to baseline DSSRM. It is also observed that unlike 12/10 pole DSSRM; 24/20 pole DSSRM is supine to the shift of rotor segments in the view of mechanical vibration in the motor. The parameters of the motor will be optimized for the prototype machine and it will be built in the future.

REFERENCES

[1] J. Nerg, M. Rilla, V. Ruuskanen, J. Pyrhonen, and S. Ruotsalainen, "Direct-driven interior magnet permanent-magnet synchronous motors for a full electric sports car," *IEEE Trans. Ind. Electron.*, vol. 61, no. 8, pp. 4286–4294, Aug. 2014.

[2] R. R. Kumar, P. Devi, C. Chetri, A. S. S. Vardhan, R. M. Elavarasan, L. Mihet-Popa, and R. K. Saket, "Design and characteristics investigation of novel dual stator pseudo-pole five-phase permanent magnet synchronous generator for wind power application," *IEEE Access*, vol. 8, pp. 175788–175804, 2020.

[3] R. R. Kumar, S. K. Singh, R. K. Srivastava, A. S. S. Vardhan, R. M. Elavarasan, R. K. Saket, and E. Hossain, "Modeling of airgap fluxes and performance analysis of five phase permanent magnet synchronous generator for wind power application," *IEEE Access*, vol. 8, pp. 195472–195486, 2020.

[4] D. Gerada, A. Mebarki, N. L. Brown, C. Gerada, A. Cavagnino, and A. Boglietti, "High-speed electrical machines: Technologies, trends, and developments," *IEEE Trans. Ind. Electron.*, vol. 61, no. 6, pp. 2946–2959, Jun. 2014.

[5] A. Chiba, K. Kiyota, N. Hoshi, M. Takemoto, and S. Ogasawara, "Development of a Rare-Earth-Free SR motor with high torque density for hybrid vehicles," *IEEE Trans. Energy Convers.*, vol. 30, no. 1, pp. 175–182, Mar. 2015.

[6] F. Yi and W. Cai, "A quasi-Z-source integrated multiport power converter as switched reluctance motor drives for capacitance reduction and wide-speed-range operation," *IEEE Trans. Power Electron.*, vol. 31, no. 11, pp. 7661–7676, Nov. 2016.

[7] M. Ma, Z. Chang, Y. Hu, F. Li, C. Gan, and W. Cao, "An integrated switched reluctance motor drive topology with voltage-boosting and on-board charging capabilities for plug-in hybrid electric vehicles (PHEVs)," *IEEE Access*, vol. 6, pp. 1550–1559,2018.

[8] Q. Sun, J. Wu, C. Gan, Y. Hu, N. Jin, and J. Guo, "A new phase current reconstruction scheme for four-phase SRM drives using improved converter topology without voltage penalty," *IEEE Trans. Ind. Electron.*, vol. 65, no. 1, pp. 133–144, Jan. 2018.

[9] A. K. Mishra and B. Singh, "Self-governing single-stage photovoltaic water pumping system with voltage balancing control for a four-phase SRM drive," *IET Electr. Power Appl.*, vol. 14, no. 1, pp. 119–130, Jan. 2020.

[10] R. Todd, V. Valdivia, F. J. Bryan, A. Barrado, A. Lázaro, and A. J. Forsyth, "Behavioural modelling of a switched reluctance motor drive for aircraft power systems," *IET Electr. Syst. Transp.*, vol. 4, no. 4, pp. 107–113, Dec. 2014.

[11] J. Liang, L. Jian, G. Xu, and Z. Shao, "Analysis of electromagnetic Behavior in switched reluctance motor for the application of integrated air conditioner on-board charger system," *Prog. Electromagn. Res.*, vol. 124, pp. 347–364, 2012.

[12] K. Isobe, K. Nakamura, and O. Ichinokura, "A consideration of high-speed SR motor for electric power tools," *J. Magn. Soc. Jpn.*, vol. 38, no. 5, pp. 194–198, 2014.

[13] H. Hayashi, K. Nakamura, A. Chiba, T. Fukao, K. Tungpimolrut, and D. G. Dorrell, "Efficiency improvements of switched reluctance motors with high-quality iron steel and enhanced conductor slot fill," *IEEE Trans. Energy Convers.*, vol. 24, no. 4, pp. 819–825, Dec. 2009.

[14] P. C. Desai, M. Krishnamurthy, N. Schofield, and A. Emadi, "Novel switched reluctance machine configuration with higher number of rotor poles than stator poles: Concept to implementation," *IEEE Trans. Ind. Electron.*, vol. 57, no. 2, pp. 649–659, Feb. 2010.

[15] B. C. Mecrow, E. A. El-Kharashi, J. W. Finch, and A. G. Jack, "Segmental rotor switched reluctance motors with single-tooth windings," *IEE Proc.-Electr. Power Appl.*, vol. 150, no. 5, pp. 591–599, Sep. 2003.

[16] N. S. Prakash, R. V. Prabhakar, and B. G. Fernandes, "A segmented switched reluctance motor as hub drive for an electric vehicle," Indian Patent 331 582 B, Sep. 20, 2011.

[17] C. H. Perry, "Switched reluctance motor and switched reluctance apparatus for hybrid vehicles," U.S. Patent, 10 075 050 B2, Mar. 26, 2015.

[18] P. Boaventura-Delanoe, "Switched reluctance permanent magnet motor," U.S. Patent 9 831 753 B2, Apr. 14, 2016.

[19] E. Cosoroaba, E. Bostanci, Y. Li, W. Wang, and B. Fahimi, "Comparison of winding configurations in double-stator switched reluctance machines," *IET Electr. Power Appl.*, vol. 11, no. 8, pp. 1407–1415, 2017.

[20] E. Bostanci, M. Moallem, A. Parsapour, and B. Fahimi, "Opportunities and challenges of switched reluctance motor drives for electric propulsion: A comparative study," *IEEE Trans. Transport. Electrific.*, vol. 3, no. 1, pp. 58–75, Mar. 2017.

[21] J. Zhang, H. Wang, L. Chen, C. Tan, and Y. Wang, "Multi-objective optimal design of bearingless switched reluctance motor based on multi-objective genetic particle swarm optimizer," *IEEE Trans. Magn.*, vol. 54, no. 1, pp. 1–13, Jan. 2018.

[22] Y. Huang, F. Huang, Y. Yuan, F. Yang, and K. Xie, "Design and analysis of a novel bearingless segmented switched reluctance motor," *IEEE Access*, vol. 7, pp. 94342–94349, 2019.

[23] C. Gan, J. Wu, M. Shen, S. Yang, Y. Hu, and W. Cao, "Investigation of skewing effects on the vibration reduction of three-phase switched reluctance motors," *IEEE Trans. Magn.*, vol. 51, no. 9, pp. 1–9, Sep. 2015.

[24] T. Celik, "Segmental rotor switched reluctance drive," Ph.D. dissertation, School Elect., Electron. Comput. Eng., Newcastle Univ., Tyne, U.K., Aug. 2011.

[25] X. Deng, B. Mecrow, H. Wu, and R. Martin, "Design and development of low torque ripple variable-speed drive system with six-phase switched reluctance motors," *IEEE Trans. Energy Convers.*, vol. 33, no. 1, pp. 420–429, Mar. 2018.

[26] M. Aydin, Z. Q. Zhu, T. A. Lipo, and D. Howe, "Minimization of cogging torque in axial-flux permanent-magnet machines: Design concepts," *IEEE Trans. Magn.*, vol. 43, no. 9, pp. 3614–3622, Sep. 2007.

[27] R. Madhavan and B. G. Fernandes, "Performance improvement in the axial flux-segmented rotor-switched reluctance motor," *IEEE Trans. Energy Convers.*, vol. 29, no. 3, pp. 641–651, Sep. 2014.

[28] M. J. Kermanipour and B. Ganji, "Modification in geometric structure of double-sided axial flux switched reluctance motor for mitigating torque ripple," *Can. J. Electr. Comput. Eng.*, vol. 38, no. 4, pp. 318–322, 2015.

[29] Q. Sun, J. Wu, C. Gan, C. Shi, and J. Guo, "DSSRM design with multiple pole arcs optimization for high torque and low torque ripple applications," *IEEE Access*, vol. 6, pp. 27166–27175, 2018.

[30] N. Tojima, T. Jikumaru, N. Handa, K. Ishimoto, G. Kuwata, S. Ohashi, and T. Hirao, "Double stator switched reluctance rotating machine," U.S. Patent 10 367 398 B2, Sep. 29, 2016.

[31] M. Abbasian, M. Moallem, and B. Fahimi, "Double-stator switched reluctance machines (DSSRM): Fundamentals and magnetic force analysis," *IEEE Trans. Energy Convers.*, vol. 25, no. 3, pp. 589–597, Sep. 2010.

[32] W.-S. Yao, "Rapid optimization of double-stators switched reluctance motor with equivalent magnetic circuit," *Energies*, vol. 10, no. 10, p. 1603, Oct. 2017.

[33] T. J. E. Miller, *Switched Reluctance Motors Their Control*. London, U.K.: CRC Press, 1993.

[34] P. N. Materu and R. Krishnan, "Estimation of switched reluctance motor losses," *IEEE Trans. Ind. Appl.*, vol. 28, no. 3, pp. 668–679, Jun. 1992.

[35] C. Mademlis and I. Kioskeridis, "Performance optimization in switched reluctance motor drives with online commutation angle control," *IEEE Trans. Energy Convers.*, vol. 18, no. 3, pp. 448–457, Sep. 2003.

TRIPURARI DAS GUPTA received the B.Tech. degree in electrical and electronics engineering from the Krishna Institute of Engineering and Technology, Ghaziabad, India, in 2011, and the M.Tech. degree from the Department of Electrical Engineering, Indian Institute of Technology (BHU) Varanasi, India, in 2014, where he is currently pursuing the Ph.D. degree. He is currently also an Assistant Professor with the Department of Electrical and Electronics Engineering, Nalanda College of Engineering, Nalanda, India. His current research interest includes switched reluctance machine design and analysis.

KALPANA CHAUDHARY (Senior Member, IEEE) was born in Gwalior (MP), India, in January 1976. She received the B.E. degree in electrical engineering from the Madhav Institute of Technology and Science, Gwalior (MP), India, in 1997, the M.Tech. degree from the Indian Institute of Technology, New Delhi, India, in 1999, and the Ph.D. degree from the Indian Institute of Technology (BHU), Varanasi (UP), India, in 2009. She is a Fellow of the Institution of Engineers (India). She has published more than 25 scientific articles, book chapters, and research papers in indexed international journals and prestigious conference proceedings. She has published a book as a sole author and three book chapters. She has supervised more than 40 M.Tech. thesis and a Ph.D. thesis. At present, she is an Associate Professor with the Department of Electrical Engineering of Indian Institute of Technology (BHU), Varanasi (UP), India. Her research interests include electrical machines and drives, power electronics, and renewable energy systems.

RAJVIKRAM MADURAI ELAVARASAN received the B.E. degree in electrical and electronics engineering from Anna University, Chennai, India, and the M.E. degree in power system engineering from the Thiagarajar College of Engineering, Madurai. He worked as an Associate Technical Operations at the IBM Global Technology Services Division. He was a gold medalist in his master's degree. He worked as an Assistant Professor with the Department of Electrical and Electronics Engineering, Sri Venkateswara College of Engineering, Chennai. He currently works as a Design Engineer with the Electrical and Automotive Parts Manufacturing Unit, AA Industries, Chennai. He also works as a Visiting Scholar the with Clean and Resilient Energy Systems (CARES) Laboratory, Texas A&M University, Galveston, USA. He has published papers in international journals, and international and national conferences. His areas of interest include solar PV cooling techniques, renewable energy and smart grids, wind energy research, power system operation and control, artificial intelligence, control techniques, and demand-side management. He is a recognized reviewer in reputed journals, namely IEEE SYSTEMS, IEEE ACCESS, IEEE COMMUNICATIONS MAGAZINE, *International Transactions on Electrical Energy Systems (Wiley), Energy Sources, Part A: Recovery, Utilization and Environmental Effects (Taylor and Francis), Scientific Reports (Springer Nature), Chemical Engineering Journal (Elsevier), and CFD Letters and Biotech (Springer).*

R. K. SAKET (Senior Member, IEEE) is currently a Professor with the Department of Electrical Engineering, Indian Institute of Technology (Banaras Hindu University) Varanasi, India. Previously, he was a faculty member with the Birla Institute of Technology and Science, Pilani (Rajasthan), India; University Institute of Technology, Rajiv Gandhi University of Technology, Bhopal (Madhya Pradesh), India, and Sam Higginbottom University of Agriculture, Technology and Sciences, Allahabad (UP), India. He has more than twenty years of academic and research experience. He is the author / coauthor of approximately 125 scientific articles, book chapters, and research papers in indexed international journals and prestigious conference proceedings.

Dr. Saket is a Fellow of the Institution of Engineers (India); Senior Member of IEEE (USA); Member of IET (UK), and a Life Member of the Indian Society for Technical Education, New Delhi (India). He is an Editorial Board Member of the *IET Renewable Power Generation (UK); Journal of Electrical Systems (France), and Engineering, Technology and Applied Science Research*, Greece. He has received many awards, honors, and recognitions for his academic and research contributions including the prestigious Gandhian Young Technological Innovation Award–2018 by the Hon'ble President of India at New Delhi, India, Design Impact Award–2018 by Padma Vibhushan Ratan Tata at Mumbai, India, and Nehru Encouragement Award–1988 and 1990 by Hon'ble Chief Minister of M.P. State Government, Bhopal, India. His research interests include reliability engineering, electrical machines and drives, power system reliability, and renewable energy systems.

IRFAN KHAN (Senior Member, IEEE) received the Ph.D. degree in electrical and computer engineering from Carnegie Mellon University, USA. He is currently an Instructional Assistant Professor with the Marine Engineering Technology Department in a joint appointment with the Electrical and Computer Engineering Department of Texas A&M University (TAMU) TX USA. His current research interests include the control and optimization of smart energy networks, optimization of energy storage systems, DC microgrids, smart grids, and renewable energy resources. He has published more than 40 refereed journal and conference papers in the smart energy systems related areas. He is the Vice-Chair for the IEEE PES Joint chapter of Region 5 Galveston Bay Section (GBS). He was the Registration Chair at IEEE sponsored International Symposium on Measurement and Control in Robotics that was organized at the University of Houston Clear Lake in September 2019. He has served several electrical engineering journals as guest editors.

EKLAS HOSSAIN (Senior Member, IEEE) received the B.S. degree in electrical and electronic engineering from the Khulna University of Engineering and Technology, Bangladesh, in 2006, the M.S. degree in mechatronics and robotics engineering from the International Islamic University of Malaysia, Malaysia, in 2010, and the Ph.D. degree from the College of Engineering and Applied Science, University of Wisconsin Milwaukee (UWM). He has been working in the area of distributed power systems and renewable energy integration for last ten years and he has published a number of research papers and posters in this field. He is now involved with several research projects on renewable energy and grid tied microgrid system at Oregon Tech, as an Assistant Professor with the Department of Electrical Engineering and Renewable Energy since 2015. He is currently serving as an Associate Editor of the IEEE ACCESS. His research interests include modeling, analysis, design, and control of power electronic devices; energy storage systems; renewable energy sources; integration of distributed generation systems; micro grid and smart grid applications; robotics, and advanced control system. He, with his dedicated research team, is looking forward to explore methods to make the electric power systems more sustainable, cost-effective and secure through extensive research and analysis on energy storage, micro grid system, and renewable energy sources.

● ● ●